THE ROLE OF SHEAR HEATING IN PRODUCING CRYSTAL-POOR OBSIDIAN

Adam C. Curry

A thesis submitted to the faculty of the University of North Carolina at Chapel Hill in partial fulfillment of the requirements for the degree of Master of Science in the Department of Geological Sciences.

Chapel Hill
2013

Approved by:

Allen F. Glazner

Drew S. Coleman

Kevin G. Stewart

Eric B. Grosfils

ABSTRACT

Adam Curry: The role of shear heating in producing crystal-poor obsidian
(Under the direction of Allen F. Glazner)

The reasons for obsidian's lack of phenocrysts (<1 vol%) are poorly understood. Modal analyses of obsidian from the Long Valley and Coso volcanic areas in California were completed to better understand the crystallization history of obsidian. Crystal-poor samples (< 2 vol%) contain plagioclase but lack sanidine and often quartz, whereas crystal-rich samples (>2 vol%) contain plagioclase and sanidine but sometimes lack quartz. Crystal-poor samples contain dominantly rounded phenocrysts indicative of resorption, whereas phenocrysts in crystal-rich samples contain sharp, defined corners. Thermal models of ascending, high-silica magma were run using COMSOL Multiphysics to assess temperature increases caused by shear heating, which could potentially resorb crystals. Models show large (>300 K) temperature increases at the conduit edges capable of resorbing crystals. Though model dike geometry is unrealistic, obsidian mineralogy and thermal modeling are consistent with shear heating-induced resorption during ascent of high-silica magmas.

ACKNOWLEDGEMENTS

TABLE OF CONTENTS

LIST OF TABLES

LIST OF FIGURES

LIST OF ABBREVIATIONS AND SYMBOLS

a	pre-exponential constant (K^{-1})
al	allanite
an	anorthoclase
ap	apatite
bt	biotite
C	Celsius
C_p	specific heat ($J\ kg^{-1}\ K^{-1}$)
CP	crystal-poor
CR	crystal-rich
dP/dy	pressure change over conduit length ($Pa\ m^{-1}$)
F	volume force ($N\ m^{-3}$)
fay	fayalite
G	Gruntfest number
G''	modified Gruntfest number
h	half-width of planar conduit (m)
hb	hornblende
I	identity tensor
K	Kelvin
k	thermal conductivity ($W\ m^{-1}\ K^{-1}$)
l	half-thickness of a lava flow (m)
L	conduit length (m)
Ma	million years ago

mt	magnetite
opx	orthopyroxene
plg	plagioclase
pyr	pyrrhotite
qz	quartz
T	temperature
t	time
u	velocity ($m\,s^{-1}$)
vol%	volume percent
wt%	weight percent
zr	zircon
γ	shear rate (s^{-1})
ΔP	conduit overpressure; P_0 (inlet)-P_1 (outlet) (MPa)
ε	shear heating ($W\,m^{-3}$)
η	viscosity (Pa s)
ρ	density ($kg\,m^{-3}$)
σ	constant shear stress (Pa)
τ	viscous stress (Pa)

1. INTRODUCTION

Obsidian is unusual because of its dearth of phenocrysts, typically <1 vol% (e.g., Bacon et al., 1981), and little is known about its formation. Magmas that erupt have usually experienced some crystallization, and most volcanic rocks contain 15-35 vol% phenocrysts (Williams et al., 1954; Ewart, 1976). The few phenocrysts in obsidian are evidence for some crystallization, but the relative paucity reflects conditions in which crystallization was inhibited or existing crystals were resorbed during ascent. The causes of these conditions and their effect on the mineralogy of obsidian are poorly understood.

Most rhyolites contain quartz, alkali feldspar, and plagioclase ± hornblende, biotite, and pyroxene (e.g., Lipman et al., 1978; Johnson and Lipman, 1988; Christiansen, 2001). Rhyolites typically plot near the haplogranite ternary cotectic (Tuttle and Bowen, 1958), and the equilibrium cotectic mineral assemblage is quartz and one or two alkali feldspars. However, many obsidian flows in eastern California lack either quartz or sanidine (Bailey et al., 1976; Kelleher, 1986; Metz and Mahood, 1991; Manley and Bacon, 2000). The lack of this cotectic mineral assemblage means either 1) quartz and sanidine never crystallized in equilibrium at this cotectic or 2) equilibrium conditions were subsequently disrupted, causing resorption of existing crystals.

One way to inhibit crystallization and resorb crystals is to increase temperature. Temperature increase is usually associated with heat from external sources, such as magma mixing or ponding of mafic magma (e.g., Stimac and Wark, 1992), but it can also be produced within a system by viscous heating. Viscous heating is the production of thermal

energy from shear stress in a moving fluid (Gruntfest, 1963; Batchelor, 1967). Because of their high viscosities (10^6-10^{12} Pa s, Figure 1), rhyolites are more susceptible to this effect than less viscous magmas, and it is potentially an important factor in the thermal budget of ascending high-silica magmas. Even though viscous heating has been studied theoretically for 50 years or more (Gruntfest, 1963; Fujii and Uyeda, 1974), its application to volcanology is relatively recent (e.g., Polacci et al., 2001; Mastin, 2005; Kendrick et al., 2012).
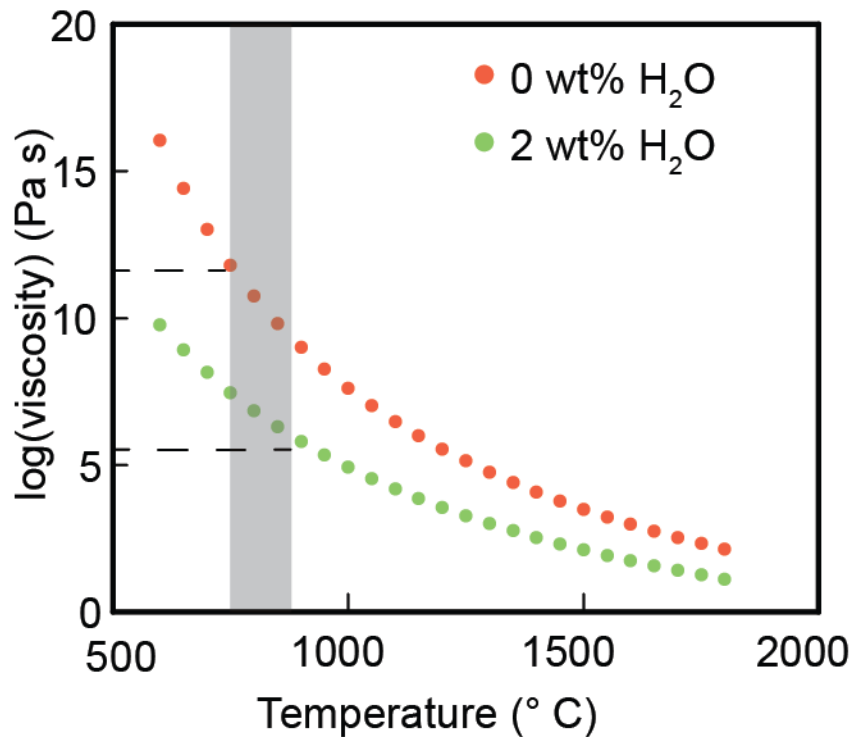
Figure 1. Viscosity (Pa s) as a function of temperature (° C) for crystal-free, high-silica rhyolite (77 wt% SiO_2) with 0 and 2 wt% H_2O. The highlighted portion shows that viscosity ranges from ~10^6-10^{12} Pa s at temperatures relevant to rhyolite melts (~750-850° C). Viscosity values were calculated using Giordano et al. (2008).

Recent studies documented the effects of viscous heating in experimental, numerical, and physical volcanology. Numerical models of magmatic conduit flow calculated temperature increases of 100-350 K at the conduit edge (Mastin, 2005; Costa et al., 2007; Hale et al., 2007). Lavallee et al. (2012) experimentally produced viscous melt by shearing an andesite to explore the movement of andesitic plugs, and Kendrick et al. (2012) attributed

rounded crystals in high-shear zones of volcanic spines extruded at Mount St. Helens to viscous heating. The role of shear heating in volcanic systems is increasingly being explored, but its application to magma crystallization and resorption is still poorly studied.

This study merges numerical models with mineralogical observations to investigate the importance of shear heating in the generation of crystal-poor obsidian. Models of ascending, high-silica magma were built in COMSOL Multiphysics to assess temperature increases within volcanic conduits. Obsidian from the Long Valley and Coso volcanic areas in eastern California was collected for modal analysis to understand the crystallization history of obsidian. This combination of mineralogy and numerical modeling provides insight into whether obsidian mineralogy is consistent with a temperature increase caused by shear heating.

2. BACKGROUND

2.1 Geologic background

The Long Valley and Coso volcanic areas are located east of the Sierra Nevada in California. Long Valley is ~25 km south of Mono Lake, and the Coso volcanic field lies between the southern Sierra Nevada and the Argus Range. Both are located at the western edge of the Basin and Range extensional province in eastern California (Figure 2).

The elliptical Long Valley caldera is 32 km by 17 km, and formed 0.767 Ma with eruption of the Bishop Tuff (Bailey et al., 1976; Crowley et al., 2007). Intra-caldera rhyolites (74-75 wt% SiO_2) comprising the resurgent dome erupted during the 0.1 million years following the Bishop Tuff eruption (K-Ar ages of 0.73-0.63 Ma, Bailey et al., 1976). Phenocryst contents for each study site are listed in Table 1 and range from 0-8 vol%.

Glass Mountain, on the northeast rim of the caldera, earned its name from the presence of abundant glassy, aphyric rhyolite. It contains over 50 rhyolite lava flows totaling ~50 km^3 which erupted between 2.1-0.79 Ma (Figure 2a; Metz and Mahood, 1991). Metz and Mahood (1991) distinguished older (2.1-1.2 Ma) and younger (1.2-0.79 Ma) lavas based on their eruptive frequency, physical character, and chemistry. Younger lavas have fewer phenocrysts than older lavas. Biotite is present in all but 2 older lavas, but only half of the younger lavas. Sanidine is present in all older lavas, but it is sparse in some younger lavas and absent in one (Metz and Mahood, 1991; Table 1).
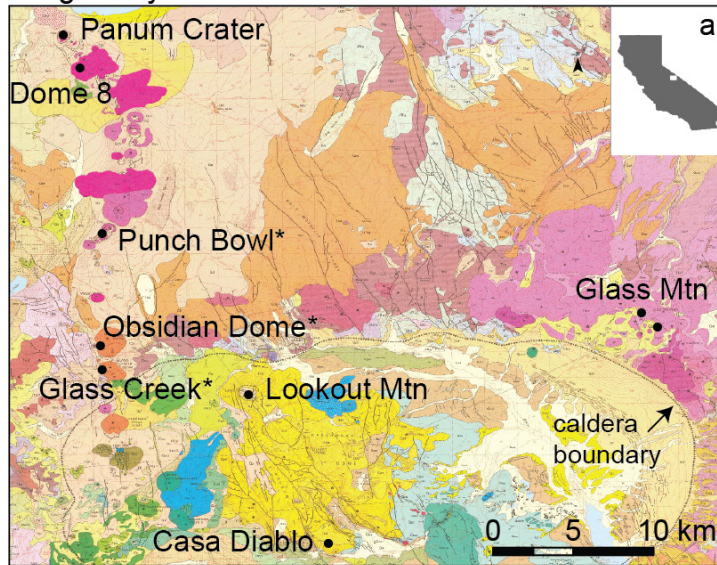
Figure 2. Geologic maps of sample sites (black dots). (a). Long Valley map adapted from Bailey (1989). Sites sampled include Panum Crater, Dome 8, and Punch Bowl in the Mono chain; Obsidian Dome and Glass Creek Dome in the Inyo chain; Lookout Mountain and Casa Diablo in the resurgent dome; and Glass Mountain. (b) Coso map adopted from Duffield and Bacon (1981). Domes 4 and 16 were sampled. Dome numbers taken from Bacon et al. (1981).

The Mono-Inyo chain of volcanic domes and craters extends north from the western part of Long Valley caldera (Figure 2a). Mono-Inyo volcanism started between 0.3 and 0.2 Ma, and the youngest features are 200 years old (Sieh and Bursik, 1986). The Mono chain consists of 27 high-silica domes and one dacitic dome (Kelleher and Cameron, 1990). The

high-silica rhyolites are divided into 3 groups: 1) aphyric with few to no phenocrysts, 2) sparsely porphyritic with ≤ 3 vol% phenocrysts, and 3) porphyritic with 3-8 vol% phenocrysts (Kelleher and Cameron, 1990). Kelleher and Cameron (1990) reported only the mineralogy of groups 2 and 3 due to the crystal-poor nature of the first group (Table 1). This study sampled one dome from each category.

Obsidian Dome and Glass Creek Dome, in the Inyo chain, formed 600 years ago (Figure 2a; Miller, 1985). These domes contain 71-74 wt% SiO_2 and consist of two units: 1) finely porphyritic obsidian with 2-6 vol% phenocrysts and 2) coarsely porphyritic rhyolite with over 18 vol% phenocrysts (Miller, 1985; Sampson and Cameron, 1987; Higgins and Meilleur, 2009). Only the finely porphyritic obsidian was analyzed in this study (Table 1).

Pleistocene volcanic rocks in the Coso volcanic field are bi-modal, predominantly either rhyolite or basalt (Figure 2b; Bacon, 1982). Pleistocene rhyolites contain 74-77 wt% SiO_2 and most contain <0.001−1 wt% crystals (Bacon et al., 1981; Table 1).

Table 1. Sample Site Mineral Assemblages

Location	Vol% phenocrysts	Phases present	Age (Ma)	Source
Glass Mountain (younger lavas)	<3 (2 units contain ~7)	plg, qz, ± san, bt, ap, zr, al	1.2-0.79	8
Resurgent Dome	<3	qz, plg, bt, opx ± ap, zr, pyr	0.75-0.65	1, 3
Mono-porphyritic	3-8	plg, san, qz, hb, mt ± fay, opx, bt	0.035-0.0007	4, 7
Inyo-finely porphyritic	2-6	plg, san ± bt, opx, mt, qz	0.006-0.0006	2, 5, 6
Coso Dome 4	1	qz, san, plg, mt, bt	0.06*	9
Coso Dome 16	<0.001	plg	0.1	9

Table 1. Mineral assemblages for sample sites in eastern California. Mineral abbreviations: plg=plagioclase, qz=quartz, bt=biotite, ap=apatite, zr=zircon, al=allanite, opx=orthopyroxene, pyr=pyrrhotite, hb=hornblende, mt=magnetite, and fay=fayalite. Sources: 1, Bailey et al. (1976); 2, Miller (1985); 3, Mankinen et al. (1986); 4, Sieh and Bursik (1986); 5, Sampson and Cameron (1987); 6, Vogel et al. (1989); 7, Kelleher and Cameron (1990); 8, Metz and Mahood (1991); 9, Manley and Bacon (2000). *Weighted mean age based on Group 4 of Manley and Bacon (2000).

2.2 Thermal modeling background

Thermal modeling of volcanic systems is inherently complicated because as magma ascends, it undergoes changes in temperature, pressure, crystal content, and gas content. Viscosity is affected by each of these changes and dominates the rheology of ascending magmas (Giordano et al., 2008). High-viscosity magmas such as rhyolites are more susceptible to viscous (or shear) heating (Nelson, 1981).

Even though many studies have numerically modeled volcanic conduits (e.g., Melnik and Sparks, 1999; Mastin, 2002; Melnik and Sparks, 2005; Massol and Jaupart, 2009), few incorporated viscous heating (e.g., Mastin, 2005; Costa et al., 2007; Hale et al., 2007). Mastin (2005), Costa et al. (2007), and Hale et al. (2007) presented models of incompressible, laminar, viscous flow in cylindrical conduits with 15-25 m radii and 5-8 km lengths. The models presented in these studies used crystal contents ranging from 0-75 vol% and water contents ranging from 1-4.9 wt%. Under these conditions, modeled temperatures increased 100-350 K above original magmatic temperature (Mastin, 2005; Costa et al., 2007; Hale et al., 2007). Similar to these studies, I model an incompressible, laminar, viscous magma. However, instead of a large-diameter, cylindrical dike, I model a 5-m wide, planar dike because this geometry is more realistic for silicic dike ascent (Petford et al., 1993).

3. METHODS

3.1 Sample collection

Samples were collected from the Long Valley and Coso volcanic areas in eastern California (Figure 2; Table 2). Of the Mono domes sampled, Panum Crater (01PAN12A) is classified as aphyric, Dome 8 (01D812A) is sparsely porphyritic, and Punch Bowl (01PB12) is porphyritic and fayalite-bearing (Kelleher and Cameron, 1990). All samples are obsidian except for 01PB12, which is a gray high-silica rhyolite.

Table 2. Sample Site Summary

Sample	Site/Dome	UTM (E,N)*
02CD11	Resurgent Dome/Casa Diablo	333128, 4168032
01LM12	Resurgent Dome/Lookout Mountain	328417, 4177444
04GM11	Glass Mountain	349775, 4181707
02AGM11	Glass Mountain	349234, 4181857
9-8-9	Coso/Dome 4	429200, 3994000
05COSO12A	Coso/Dome 16	427038, 3988840
01D812A	Mono/Dome 8	320718, 4197969
01PAN12A	Mono/Panum Crater	320145, 4199723
01PB12	Mono/Punch Bowl	322037, 4187309
02GC12A	Inyo/Glass Creek	321699, 4179418
02OD11	Inyo/Obsidian Dome	321684, 4180037

Table 2. Sample names and locations. *UTM Zone 11S, NAD83 datum.

3.2 Whole-rock geochemistry

Whole-rock chemical analyses were performed using wavelength-dispersive X-ray fluorescence at the University of North Carolina at Chapel Hill (UNC-CH) on a Rigaku Supermini X-ray fluorescence spectrometer. Fresh rock chips were powdered in a ceramic shatterbox. Loss on ignition was determined for each sample by heating ~2 g of rock powder

8

to 950° C for 1.5 hours. Ignited sample (0.9 ± 0.001 g) and flux (8.1 ± 0.001 g) consisting of 64.7 % lithium tetraborate, 35.3 % lithium metaborate, and 0.5 % lithium bromide were fused into a glass bead using a platinum crucible.

3.4 Petrography

Modal analyses were conducted by making a montage of images of a singly polished 51 mm x 75 mm thin section using an Olympus IX 81 microscope at the Microscopy Services Laboratory at UNC-CH. Images were collected on a 4x lens with unpolarized light on a motorized LEP Bioprecision Stage and stitched together using the software Metamorph. Total phenocryst percent was calculated by digitizing phenocrysts and using ImageJ (http://imagej.nih.gov/ij) to determine areal abundances. Samples were then analyzed using a Tescan Vega TS 5136 scanning electron microscope at UNC-CH with a 15 kV accelerating voltage and an absorption current of 5-10 nA. Backscattered electron images were collected from each sample to assess crystal morphology.

Quantitative mineral analyses were performed using wavelength-dispersive spectrometry on a JEOL JXA-8530F field emission electron probe microanalyzer at the Southeastern North Carolina Regional Microanalytical and Imaging Consortium at Fayetteville State University. Minerals were analyzed with a 15 kV accelerating voltage using a 10 nA probe current with a circular spot size of 1-5 μm. Matrix corrections were applied using the ZAF correction scheme. The Astimex standard mount was used for standardization of silicate minerals.

3.5 Thermal modeling

Previous studies described the potential for significant shear heating in viscous fluids with a strong temperature-dependent viscosity, such as magma, using the Gruntfest number,

G (Gruntfest, 1963; Fujii and Uyeda, 1974; Nelson, 1981). These models used an Arrhenius viscosity-temperature relationship,

$$\eta = \eta_0 e^{-a(T-T_0)},$$ (1)

in which η is the viscosity (Pa s), T is the temperature (K), a is a pre-exponential constant (K^{-1}), and η_0 and T_0 are initial values of the magma (Table 3). More sophisticated viscosity models exist (e.g., Hess and Dingwell, 1996; Giordano et al., 2008) which more accurately replicate the behavior of silicate melts over a wide range of compositions, volatile contents, and temperatures. However, Arrhenian models accurately reproduce behavior at magmatic temperatures of interest in this study.

The Gruntfest number, G, is given as (Gruntfest, 1963),

$$G = \frac{t_c}{t_\infty} = \frac{a\sigma^2 l^2}{k\eta_0},$$ (2)

in which σ is constant shear stress, l is the half-thickness of a lava flow, and k is the thermal conductivity (W m^{-1} K^{-1}; Table 3). G is the ratio of the time it takes a lava flow to cool by conduction in the absence of shear heating, t_c, to the time it takes a lava flow to reach extremely high temperatures with shear heating and no heat loss by conduction, t_∞ (Gruntfest, 1963). If t_c is short (i.e. heat is conducted away quickly) compared to t_∞, then heat can be transferred away from the lava so that shear heating does not produce large temperature increases within the lava. If t_c is long compared to t_∞, then significant temperature increases due to shear heating are possible. Gruntfest (1963) found that for $G>1$, temperatures in a lava flow can theoretically increase without bound for a given period of time, a situation known as thermal runaway.

Table 3. Variables

Symbol	Description	Range	This Study	Equation	Source
h	half-width of planar conduit (m)	1-18	2.5	3, 10	7, 10, 11
L	conduit length (m)		1000	4, 9	
ΔP	overpressure; P_0(inlet)-P_l(outlet) (MPa)	10-80	10-30	4, 5	13-15
dP/dy	pressure change over conduit length (Pa m^{-1})	10-10^7	10000-30000	3, 4, 10	6
k_m	magma thermal conductivity (W m^{-1} K^{-1})	1.3-4.2	1.5	3	3, 16
k_h	host rock thermal conductivity (W m^{-1} K^{-1})	1.5-3	2.25		12
C_p	specific heat (J kg^{-1} K^{-1})	1150-1250	1200	6	16
η_0	viscosity at T$_0$ (Pa s)	10^4-10^{14}	10^5-10^7	1-3, 10	2, 3
T_0	initial magma temperature (K)	973-1198	1123.15	1, 9	2, 8
T_s	surface temperature (K)		293.15	9	
T_{grad}	host rock temperature (K)		see Equation 9	9	
ρ_m	magma density (kg m^{-3})	2200-2350	2300		3, 16
ρ_h	host rock density (kg m^{-3})	2550-2730	2600		5, 9
a	pre-exponential constant (K^{-1})		0.015-0.025	1-3	2, 6
l	half-thickness of lava flow			2	1
G	Gruntfest number			2	1
G''	modified Gruntfest number		4-4690	3	4
t_c	time needed to cool via conduction (s)			2	1
t_∞	time needed to reach large temperatures via shear heating (s)			2	1
σ	constant shear stress			2	1
t	time (s)			6, 7	
u	velocity (m s^{-1})			6, 7	
ε	shear heating (W m^{-3})			6, 8	
I	identity tensor			7	
τ	viscous stress (Pa)			7	
F	volume force (N m^{-3})			7	
γ	shear rate (s^{-1})			8	

Table 3. Variables used in this paper. Sources for given ranges include: 1, Gruntfest (1963); 2, Shaw (1963); 3, Murase and McBirney (1973); 4, Fujii and Uyeda (1974); 5, Plouff et al. (1980); 6, Nelson (1981); 7, Eichelberger et al. (1985); 8, Hausback (1987); 9, Carle (1988); 10, Vogel et al. (1989); 11, Petford et al. (1993); 12, Spear (1993); 13, Melnik et al. (2005); 14, Costa et al. (2007); 15, Mastin et al. (2008);16, Romine et al. (2012).

Fujii and Uyeda (1974) modified G for applications to planar conduit flow (dikes), adapted here as

$$G''=\left(\frac{dP}{dy}\right)^2 \frac{ah^4}{k_m\eta_0},$$ (3)

in which h is the half-width of a planar conduit and

$$\frac{dP}{dy}=\frac{\Delta P}{L}.$$ (4)

In Equation 4, L is the length of the conduit and

$$\Delta P = P_0 - P_1,$$ (5)

in which P_0 is the pressure at the conduit inlet (Pa) and P_1 is the pressure at the outlet (Pa). Fujii and Uyeda (1974) found $G''= 6$ to be the critical value above which thermal runaway is possible. Equation 3 is the relevant version of the Gruntfest number for this study.

To understand the role of shear heating, this study varied 3 parameters in Equations 1-5: a, η_0, and ΔP. The pre-exponential constant in Equation 1, a, controls the sensitivity of viscosity to temperature changes. The range of a values for this study was determined by fitting Equation 1 to measured viscosity data for rhyolitic compositions with 0 to 6 wt% H_2O and an andesite with 2 wt% H_2O for comparison (Figure 3). Calculated a values range from 0.018-0.025 for rhyolites. Nelson (1981) used a=0.015 K^{-1} based on obsidian viscosity data of Shaw (1963). To analyze conditions relevant to rhyolite compositions, this study chose a=0.015, 0.020, and 0.025 K^{-1}.

Initial magma viscosity, η_0, was chosen based on experimentally derived viscosity values covering a wide range of temperatures and volatile contents (Shaw, 1963, 1972; Murase and McBirney, 1973). Rhyolite viscosity (10^4-10^{12} Pa s) depends on water content,

crystal content, and composition. To account for some water in the magma at depth, this study used a range of viscosities on the lower end of measured and calculated viscosities: 10^5, 10^6, and 10^7 Pa s.
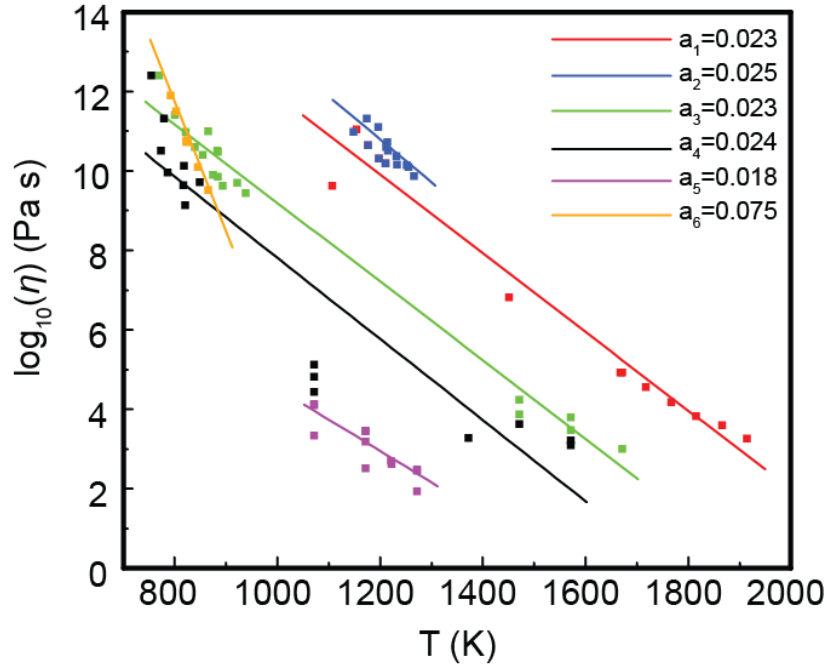
Figure 3. Regression lines for measured viscosity data of granites (a_1-a_5) and an andesite (a_6) with different water contents: a_1=0.02 wt%, a_2<1 wt%, a_3=1-1.5, a_4=1.8-3 wt%, a_5=6-8 wt%, and a_6=2 wt%. R^2=0.97, 0.68, 0.98, 0.84, 0.77, and 0.99, respectively. Data sources include Baker and Vaillancourt (1995), Hess and Dingwell (1996), Richet et al. (1996), and Dingwell et al. (1998).

The overpressure, ΔP, is the pressure difference between the inlet (P_0) and the outlet (P_1) of the conduit driving magma flow. Using geodetic models, Mastin et al. (2008) calculated magmatic overpressures of <30 MPa for the 2004-2006 Mount St. Helens eruption. Numerical models of Massol and Jaupart (1999) and Costa et al. (2007) used ΔP values ranging from 10-80 MPa to model volcanic conduit flow. Based on these studies, this study chose ΔP=10, 20, and 30 MPa.

Each combination of a (0.015, 0.020, and 0.025 K^{-1}), η_0 (10^5, 10^6, 10^7 Pa s), and ΔP (10, 20, and 30 MPa) values was run except for the combination a=0.025 K^{-1}, η_0=10^5 Pa s,

and ΔP=30 MPa due to lack of convergence in the numerical model. Twenty-six models were run, each having a specific G'' value shown in Table 4. Most models are well above the critical G''=6 value defined by Fujii and Uyeda (1974), with the exception of 2 models with η_0=10^7 Pa s.

Table 4. G" Values

η_0=10^5 Pa s				η_0=10^6 Pa s				η_0=10^7 Pa s			
ΔP (MPa)	10	20	30	ΔP	10	20	30	ΔP	10	20	30
a (K^{-1})				a				a			
0.02	391	1560	3520	0.02	39	156	352	0.02	4	16	35
0.02	521	2080	4690	0.02	52	208	469	0.02	5	21	47
0.03	651	2600		0.03	65	260	586	0.03	7	26	59

Table 4. G'' values for each thermal model run in this study.

The finite-element numerical solver COMSOL Multiphysics was used to run thermal models of high-silica magma ascending due to an overpressure at the conduit base. A planar conduit within a host rock was modeled in a symmetric half-space (Figure 4). Magma flow was modeled as an incompressible, homogenous fluid described by the following equations for conservation of energy (6) and mass (7):

$$\rho C_p \frac{\partial T}{\partial t} + \rho C_p u \cdot \nabla T = \nabla \cdot (k \nabla T) + \varepsilon$$

(6)

and

$$\rho \frac{\partial u}{\partial t} + \rho (u \cdot \nabla) u = \nabla \cdot \left[- PI + \tau \right] + F$$

, (7)

in which shear heating is defined as (Batchelor, 1967)

$$\varepsilon = 2\eta\gamma^2.$$

(8)

In Equations 6-8, ρ is density (kg m^{-3}), C_p is heat capacity (J kg^{-1} K^{-1}), T is temperature (K), t is time (s), u is velocity (m s^{-1}), k is thermal conductivity (W m^{-1} K^{-1}), P is pressure (Pa), I is the identity tensor, τ is viscous stress (Pa), F is the volume force (N m^{-3}), and γ is the shear

14

rate (s^{-1}). COMSOL was benchmarked against analytical solutions of Equations 6-7 (Appendix A).

In this study, I modeled a 5-m wide, 1000-m long rhyolite dike moving through a host rock with the thermal gradient (T_{grad}),

$$T_{grad}(y) = T_s - \left(\frac{T_0 - T_s}{L}\right)y$$

(9)

in which T_s is the surface temperature (K), T_0 is the initial magma temperature (K), and L is the conduit length in meters (Figure 4). The bottom edge of the entire model was kept at a constant T_0 to simulate a heat source at depth. The host rock changes along a linear geothermal gradient according to Equation 9 from T_0 to T_s at the surface. The host rock edge was built far (97.5 m on each side) from the conduit-host rock boundary to minimize thermal edge effects (Figure 4). I ran models for 1 year based on extrusion periods at silicic volcanoes such as Mount St. Helens and Santiaguito. Eruptions tend to be cyclic, changing in duration and intensity over periods ranging from months to years (Swanson et al., 1987; Harris et al., 2003).
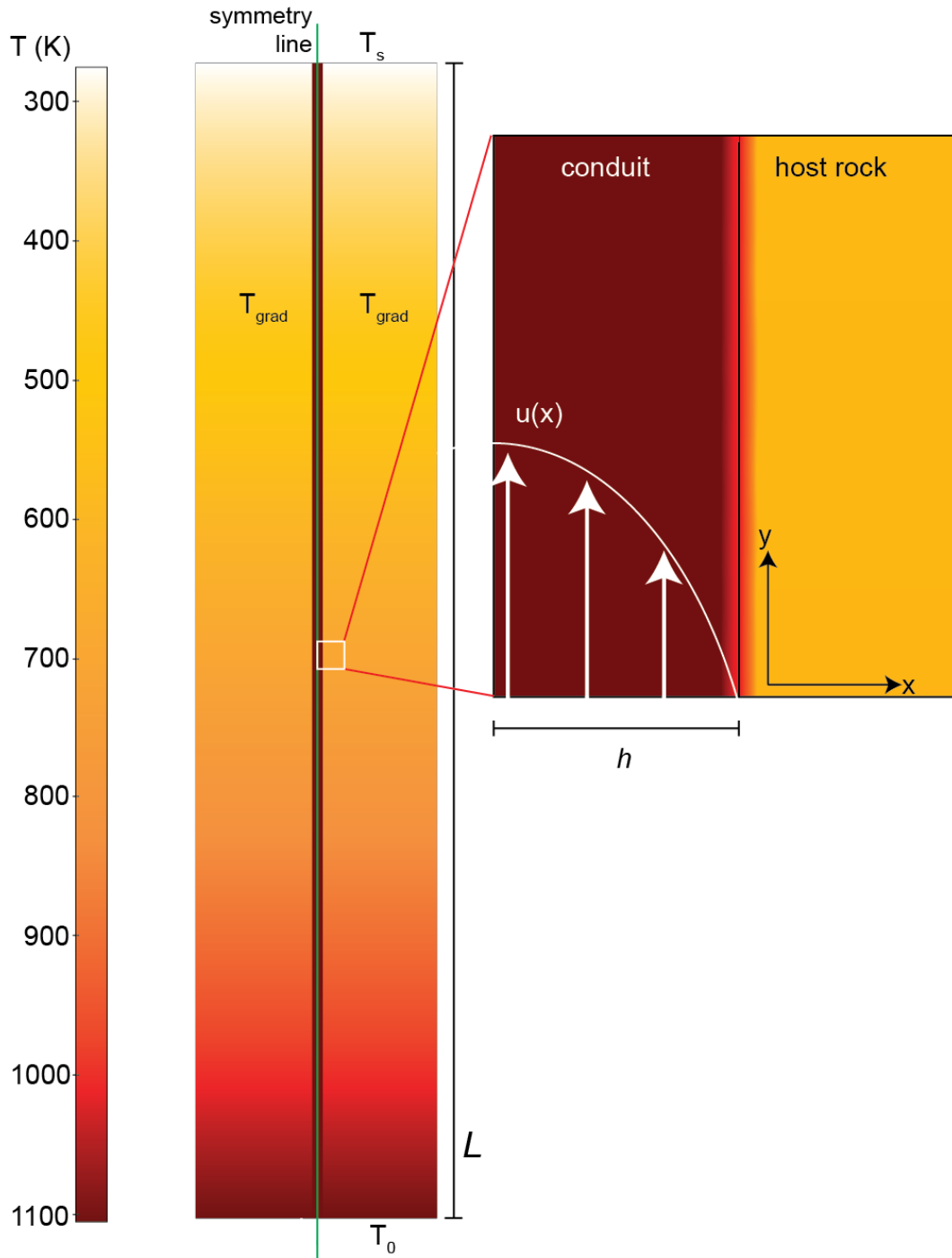
Figure 4. General setup of two-dimensional thermal model in COMSOL. A planar dike is intruded into a host rock. The bottom edge is kept at T_0 to simulate a heat source at depth, and Equation 9 describes the geothermal gradient in the host rock. This study used a symmetric half-space (symmetry line shown). Schematic parabolic velocity profile is for Poiseuille flow.

4. RESULTS

4.1 Geochemistry and modal analysis

Analyzed samples range from 72.1-78.2 wt% SiO_2 (Figure 5; Appendix B) and agree with previously published data (Rinehart and Ross, 1964; Bacon et al., 1981; Sampson and Cameron, 1987; Kelleher and Cameron, 1990; Metz and Mahood, 1991). The Inyo domes range from 70.0-75.8 wt% SiO_2, and all other sites range from 73.8-78.2 wt% SiO_2. Of the higher-silica rhyolites, Coso rhyolites have the widest range of silica values (73.8-77.5 wt% SiO_2). The resurgent dome (74.1-75.7 wt% SiO_2), Glass Mountain (76.7- 78.2 wt% SiO_2), and the Mono domes (75.4-77.0 wt% SiO_2) each have a more restricted silica range.

The oxides Al_2O_3, MgO, Fe_2O_3, TiO_2, and CaO generally decrease with increasing SiO_2. Coso samples deviate from this trend, having lower Al_2O_3 content at a given SiO_2 value than those from the Long Valley region (Figure 5). K_2O peaks at ~74 wt% SiO_2, whereas Na_2O and MnO are scattered.

Normative minerals were calculated from these analyses using the CIPW norm algorithm. Each sample contains > 90 % normative orthoclase, albite, and quartz, which are plotted in the haplogranite system in Figure 6 (Tuttle and Bowen, 1958; Brugger et al., 2003). Samples form a tight cluster except for one sample from Obsidian Dome, which is slightly poorer in quartz.
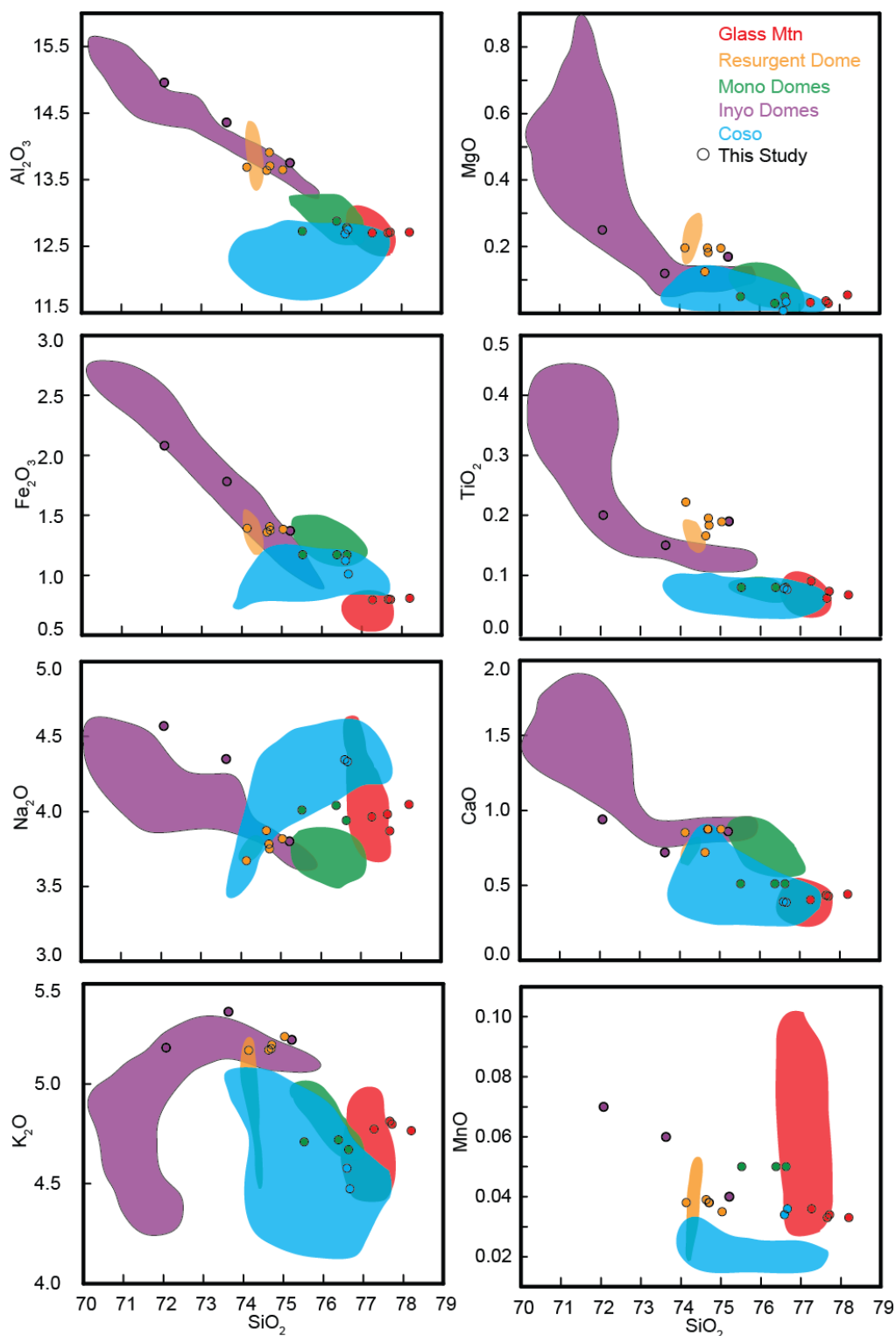
Figure 5. Geochemical data of samples from this study (circles) are consistent with previously published data (fields). Previous data are taken from Rinehart and Ross (1964), Bacon et al. (1981), Sampson and Cameron (1987), Kelleher and Cameron (1990), and Metz and Mahood (1991).

Qualitatively, obsidian can be categorized as crystal-poor (CP) or crystal-rich (CR). CP obsidian contains few to no crystals visible to the naked eye, whereas CR obsidian contains many crystals visible to the naked eye. Analyzed CP samples range from 0-1.12 vol% phenocrysts (Table 5; Figures 7-8), and analyzed CR samples range from 2.4-9.4 vol% phenocrysts (Table 5; Appendix C). Quantitatively, the cutoff for CP versus CR is ~2 vol% phenocrysts. CR data in Figure 7 are taken from Kelleher (1986) and Higgins and Meilleur (2009), and CP data collected in this study are in agreement. Only major phases are taken into account in this study.

Compositional data displayed in Figures 9 and 10 and described in this paragraph are quantitative data from a JEOL JXA-8530F field emission electron probe microanalyzer (Appendix D). CP samples contain plagioclase (An_{7-46}) with some quartz and orthopyroxene (Table 5; Figures 7-10). Orthopyroxene in the Casa Diablo sample is restricted to hypersthene (En_{55-57}). Plagioclase varies the most in Casa Diablo samples (An_{21-46}). Glass Mountain and Mono Dome 8 contain oligoclase (An_{13-17}) and a few anorthoclase, and Coso Dome 4 contains anorthoclase (An_{7-11}, Or_{7-11}). CR samples contain oligoclase (An_{10-27}), sanidine (Or_{53-68}), and quartz (Figures 7 and 10). In addition to the presence of sanidine, CR samples show a much more restricted range of plagioclase when compared to CP samples.

Table 5. Modal Analyses

Site	Vol% phenocrysts	Crystal-rich (CR) or crystal-poor (CP)	Phases present
02CD11	0.4	CP	92 % plg, 8 % opx*
01LM12	0	CP	-
04GM11	0.3	CP	plg
02AGM11	0.2	CP	plg
9-8-9	1.1	CP	59 % an, 41% qz
05COSO12A	0	CP	-
01D812A	0.1	CP	54 % qz, 46 % plg
01PAN12A	0	CP	-
01PB12	5.1	CR	see Table 1
02GC12A	2.4	CR	see Table 1
02OD11	9.4	CR	see Table 1

Table 5. Modal analyses of samples. Abbreviations: an=anorthoclase, opx=orthopyroxene, plg=plagioclase, and qz=quartz. See Appendix C for detailed modal analyses. *analyzed opx is hypersthene (En_{55}-En_{57}).
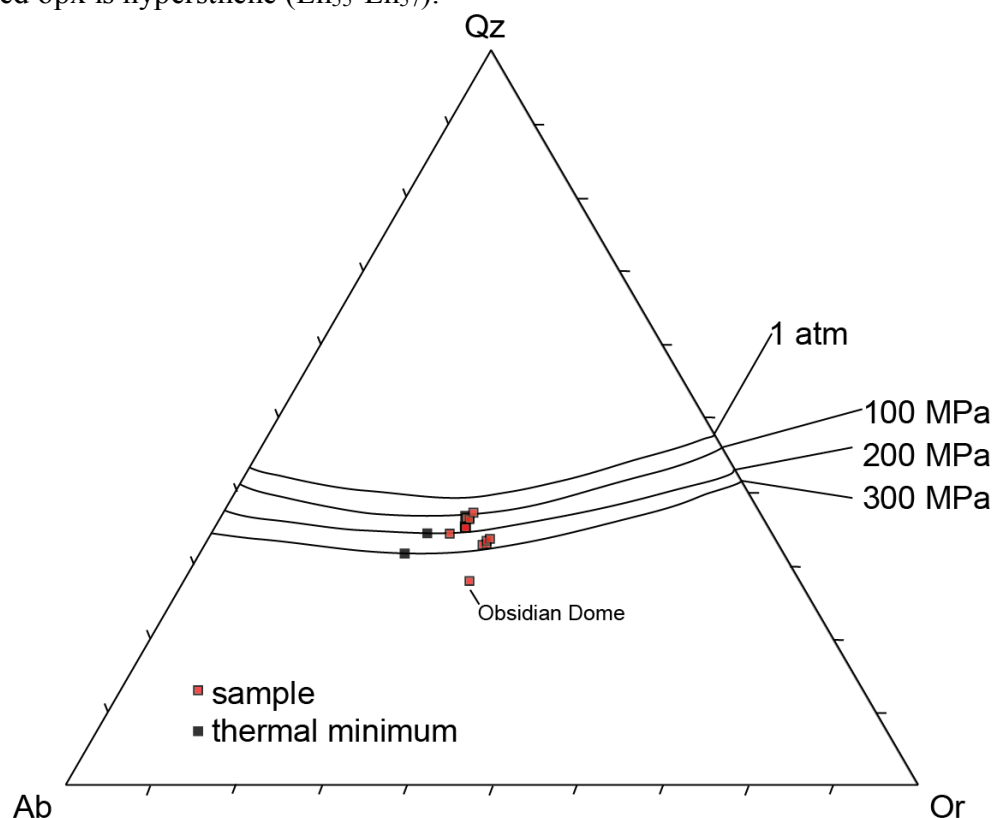
Figure 6. Samples plotted in the haplogranite system modified by Brugger et al. (2003). 300-100 MPa lines from Tuttle and Bowen (1958), and 1-atm line from Brugger et al. (2003). All samples plot fairly close on the feldspar side of the 1-atm cotectic except for a sample from Obsidian Dome which plots closer to the feldspar side.
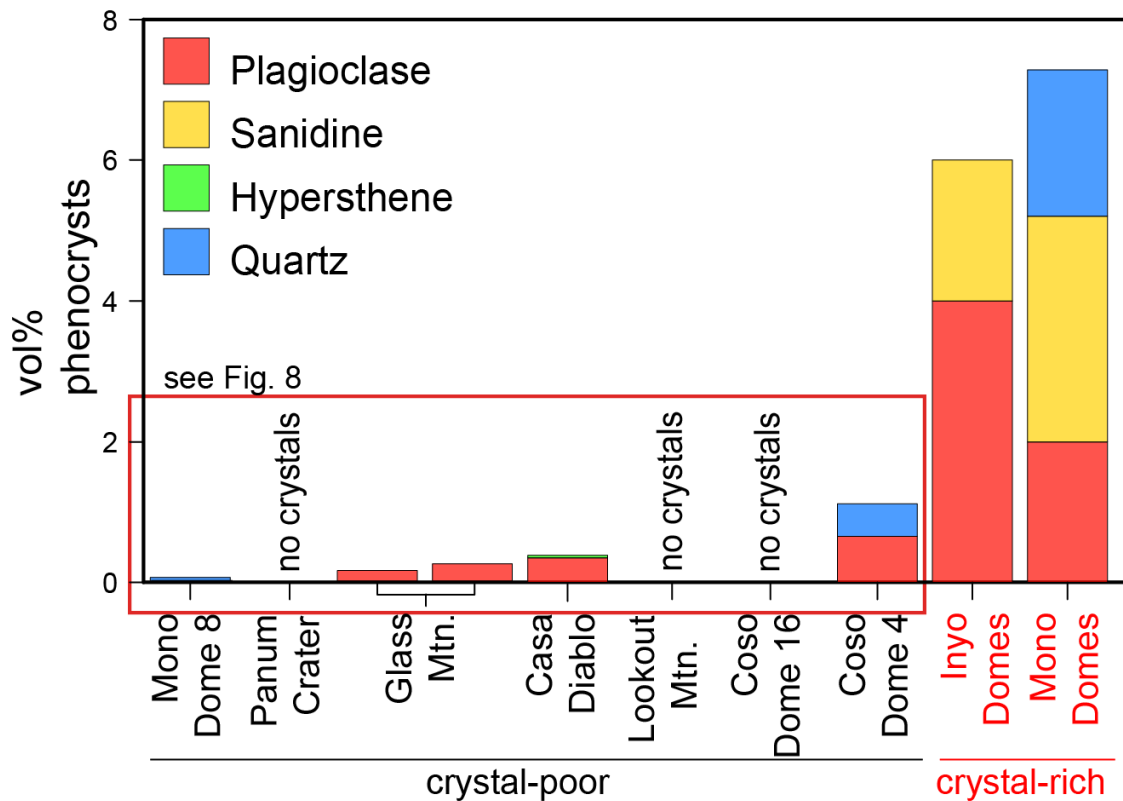
Figure 7. Modal analyses for CP and CR samples. CR data are taken from Kelleher (1986) and Higgins and Meilleur (2009). No sanidine was found in CP samples, and quartz was only found in 2 samples (Coso Dome 4 and Mono Dome 8). Anorthoclase is considered plagioclase in this figure. See Figure 8 for CP data.
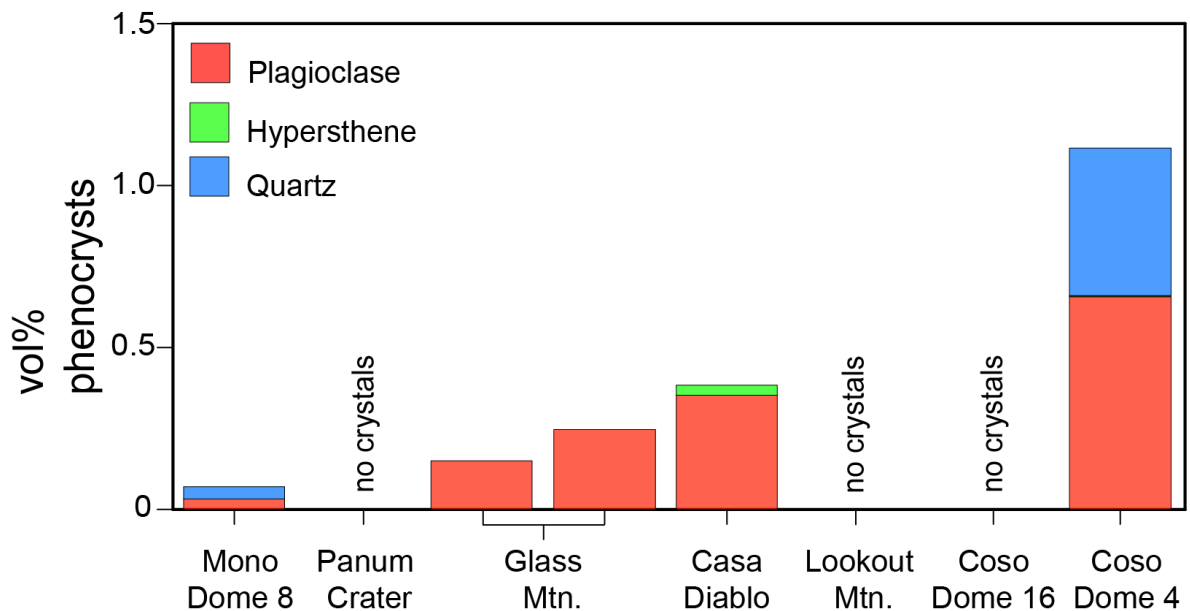
Figure 8. Modal analyses for 8 CP samples analyzed. 3 CP samples contained no phenocrysts. Plagioclase is the dominant mineral with some quartz and hypersthene (En_{55}-En_{57}) also present. Anorthoclase is considered plagioclase in this figure.

21
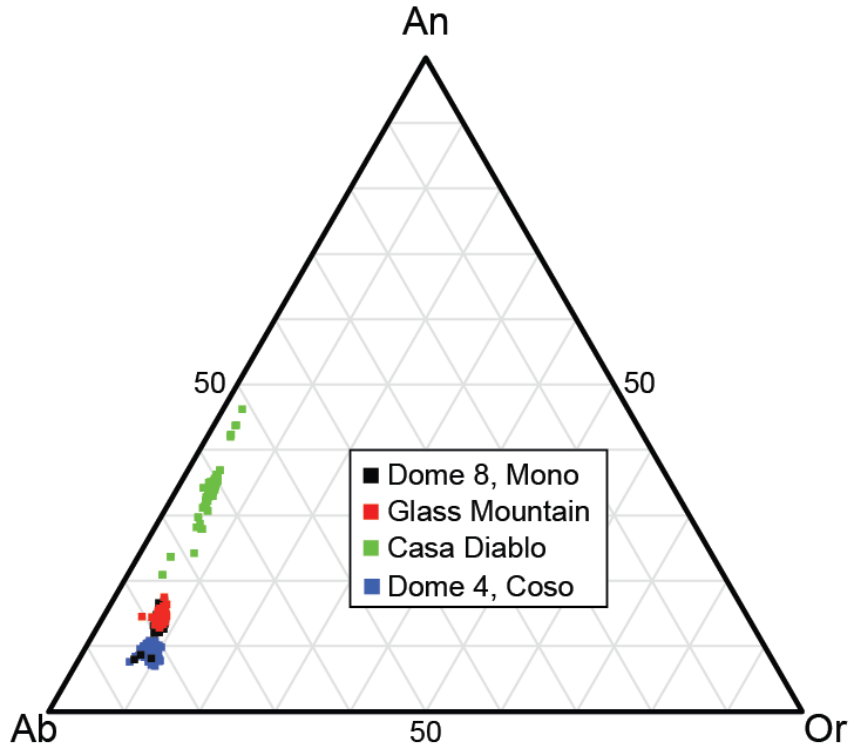
Figure 9. Feldspar compositions of CP samples. Plagioclase ranges from An_{7-46}, with Casa Diablo having the greatest range. Glass Mountain and Mono Dome 8 plot in the oligoclase field (except a few anorthoclase in Mono Dome 8), and Coso Dome 4 plots in the anorthoclase field.
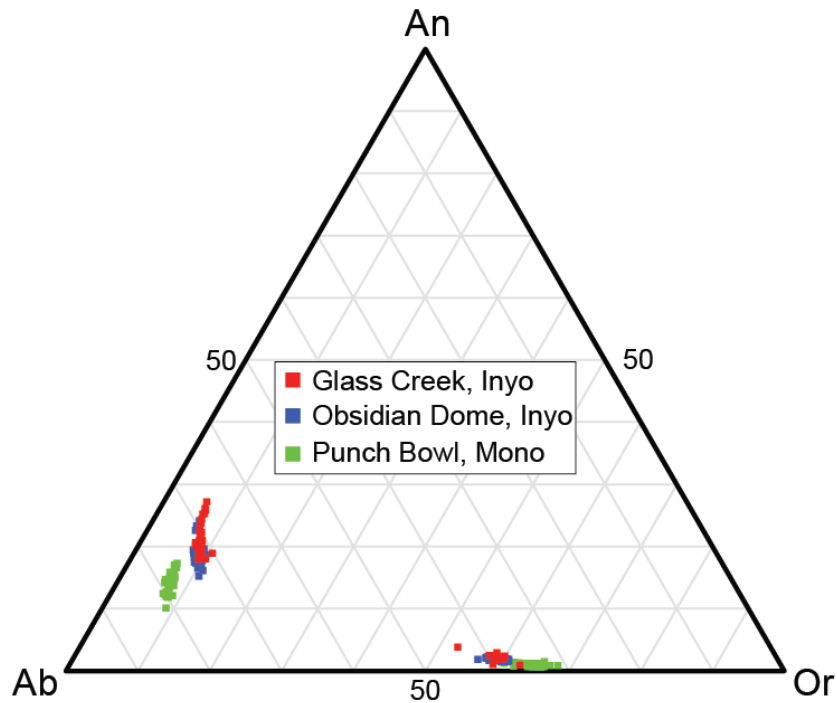
Figure 10. Feldspar compositions of CR samples. Oligoclase (An_{10-27}) and sanidine (Or_{53}-Or_{68}) compositions of CR samples from Glass Creek, Obsidian Dome, and Punch Bowl.

4.2 Crystal morphology

Phenocrysts in CP obsidian are consistently rounder than those in CR obsidian. In CP samples, hypersthene is elliptical to circular in shape, and plagioclase displays rounded corners (Figure 11). In contrast, plagioclase and alkali feldspar crystals in CR samples display planar crystal faces and sharp corners (Figure 12). Sieved plagioclase is present but not common in CP samples, but sieving is mostly absent in CR feldspars. Quartz crystals in both CP and CR samples display rounded textures, and embayments are common (Figure 13). Crystals shown in Figures 11-13 are representative of analyzed samples, and an extensive gallery of backscattered electron images is given in Appendix E. All backscattered electron images shown in this study were collected on a JEOL JXA-8530F field emission electron probe microanalyzer.
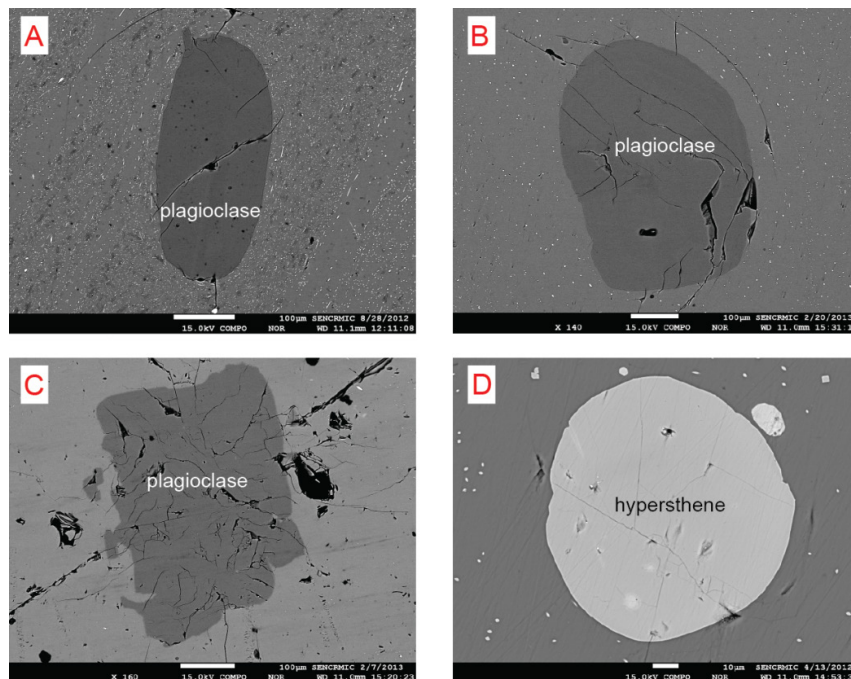
Figure 11. Backscattered electron images of CP phenocrysts, plagioclase and hypersthene. Plagioclase tends to be elongate and rounded at the corners, and hypersthene can be almost circular. These round shapes do not form during crystallization.
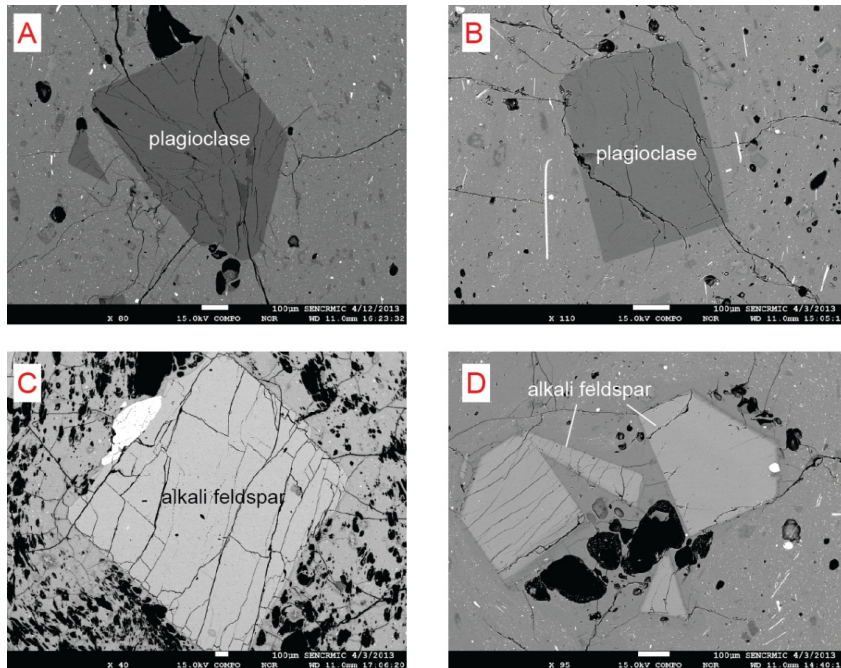
Figure 12. Backscattered electron images of CR feldspars, plagioclase and sanidine. Note the better-defined crystal shape, with sharper corners.
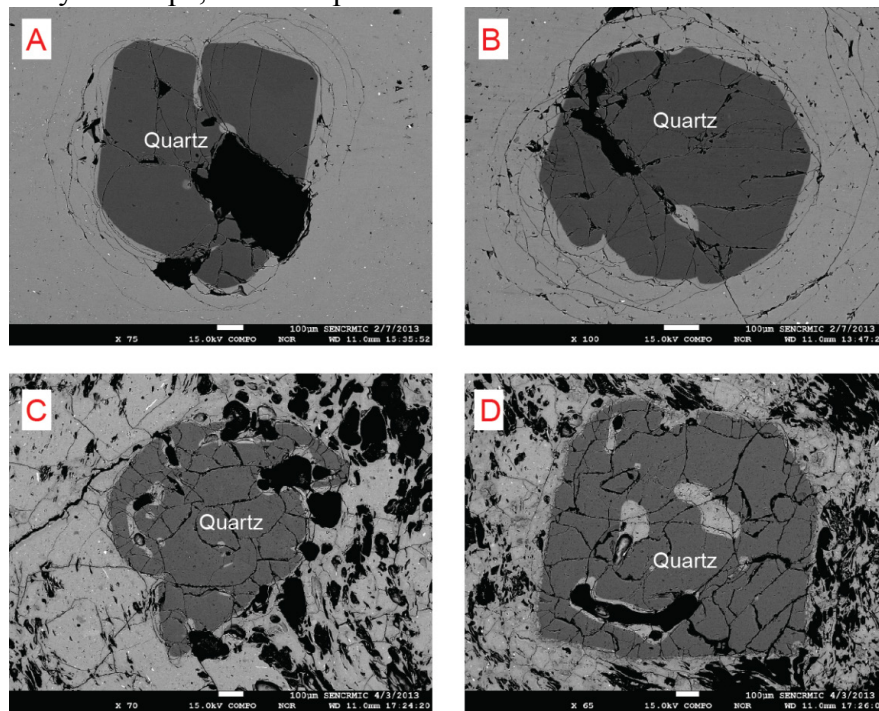
Figure 13. Backscattered electron images of quartz phenocrysts from both CP and CR samples. Unlike feldspars and pyroxene, quartz tends to show rounding and embayments in both CP and CR samples. A-B are CP, and C-D are CR.

4.3 Thermal model

In general, models behave as physically expected, meaning that increasing ΔP increases velocity, flux, and temperature rise (due to increased shear rate) for a given set of models (e.g., Table 6; Figures 14-17a). Furthermore, a is directly related to velocity and flux, but it is both directly and inversely related to temperature rise depending on ΔP and η_0 (Table 6). All models experience heat loss to the host rock via conduction, heat production via shear heating, and advection of hotter magma from the base of the conduit. These pathways of heat are the main competing factors which control model behavior.

4.3.1 Velocity

Velocity profiles (Figure 14) were calculated at the top of the conduit at t=1 yr for each model. Maximum velocities at the conduit center range from 0.003-3.35 m s^{-1}. Most velocity profiles evolve into plug-like shapes because of shear heating, which is most intense at the conduit edges due to higher shear rates. This increase in temperature reduces viscosity and allows for faster velocities.

This effect is shown in Figure 15, which shows data from Figure 14 normalized to the Poiseuille solution for velocity given by

$$u(x)_{pois} = \left(\frac{dP}{dy}\right)\frac{h^2 - x^2}{2\eta_0}.$$
(10)

Shear heating produces edge velocities much higher than would be allowed with the Poiseuille solution. Profiles in Figure 15 stop at the last mesh point before the conduit wall. Table 6c lists the maximum normalized velocity from the profiles in Figure 15.
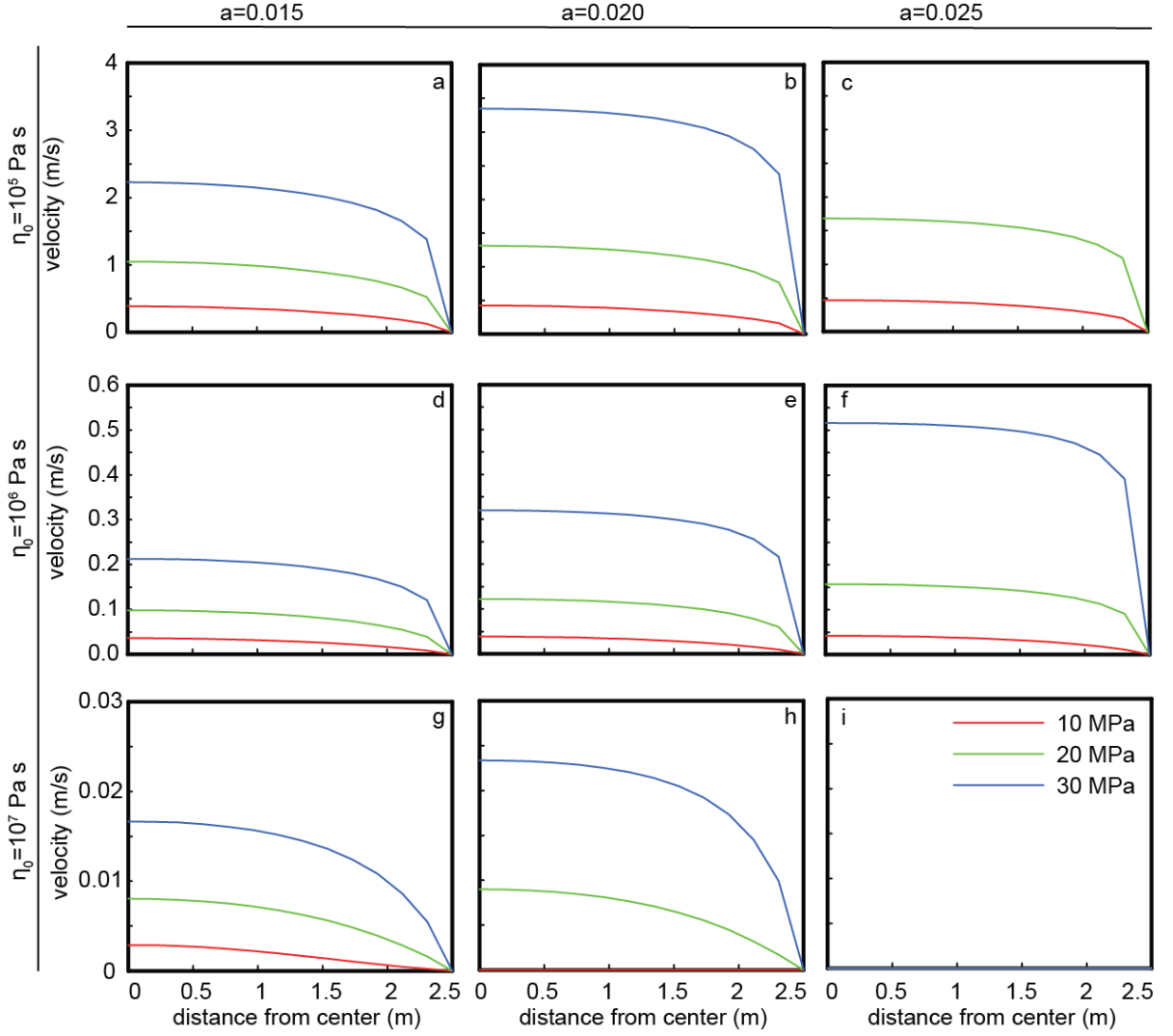
Figure 14. Velocity profiles within the conduit for all 26 models. Models in (i) are not flowing (i.e., u=0 m s^{-1}). Profiles were calculated at t=1 yr at the top of the conduit. Most models develop into plug-like shapes with high gradients at the edge and small gradients at the center due to shear heating at the edges.
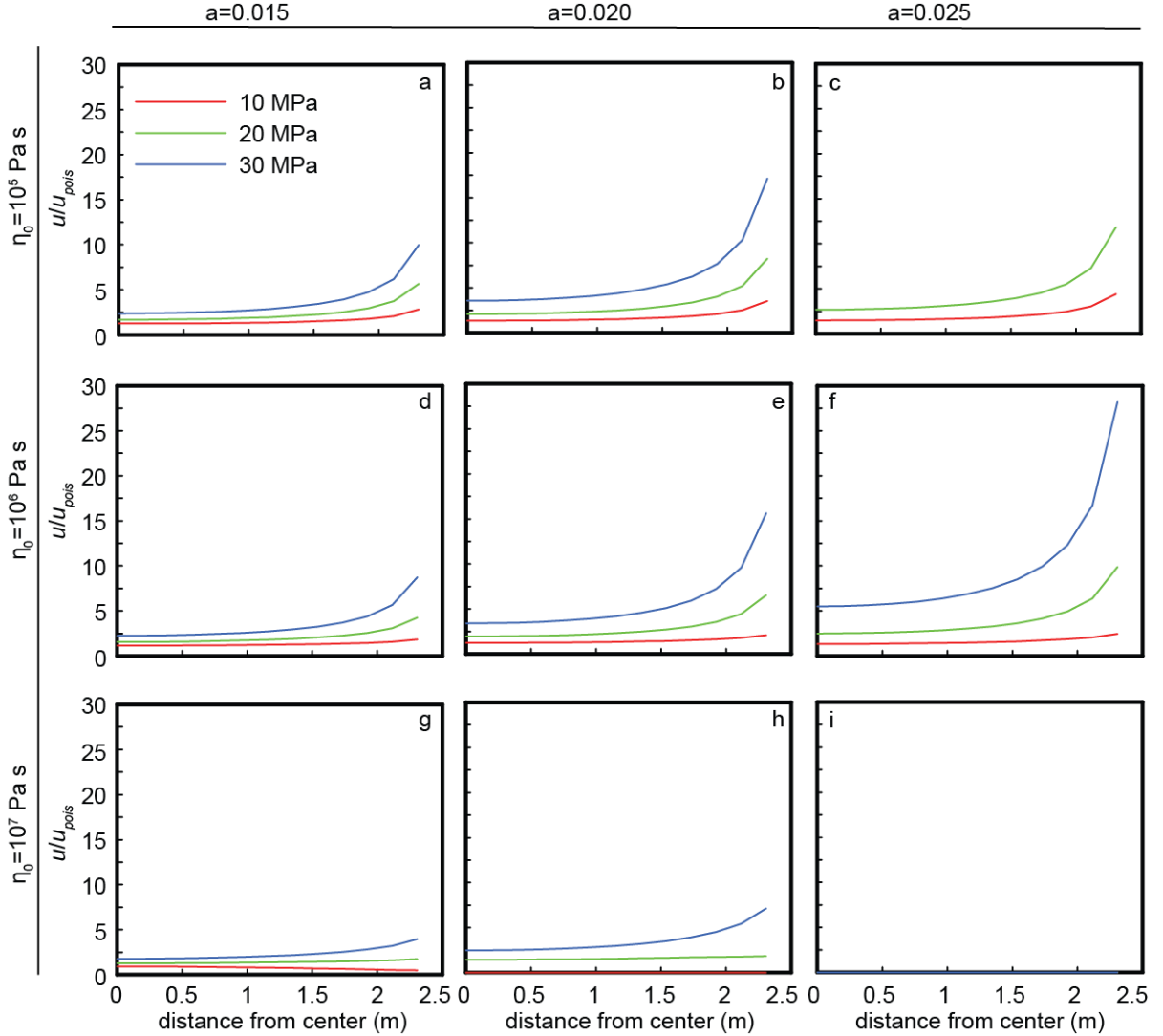
Figure 15. Normalized velocity profiles within the conduit. Velocity values from Figure 14 are normalized to the Poiseuille solution (Equation 10) to show the effect of shear heating on the edges compared to the center. Shear strain is highest near the edge, so shear heating is more prominent. This increase in temperature decreases viscosity which allows for higher velocities than the Poiseuille solution.

4.3.2 Flux

Flux was calculated by integrating the velocity over the top of the conduit, yielding units of $m^2 s^{-1}$ for this geometry (Figure 16). This calculation was made at 500 time increments in the model run time (1 yr). Figure 16 plots these discrete measurements versus the course of the 1 yr run time for the entire conduit area (not just the half-conduit).

Models can be categorized into 3 main types based on flux behavior through time: 1) models that reach a steady state of flux in <1 yr (e.g., all models with $\eta_0=10^5$ and 10^6 Pa s), 2) models whose flux is still increasing at $t=1$ yr (e.g., Figure 16g), and 3) models which shut down to a flux of 0 m^2 s^{-1} (e.g., Figure 16i). Several Type 1 and 2 models reach a flux minimum before again increasing, owing to initial heat loss by conduction. Higher viscosity (e.g., $\eta_0=10^7$ Pa s) models are more susceptible to conductive heat loss because it is harder to move magma with higher viscosities. This means that advected heat from below and viscous heating are either 1) not able to overcome conductive heat loss, causing the magma to lose heat and shut down (Type 3) or 2) able to overcome conductive heat loss after a period of time (e.g., Figure 16g models).

4.3.3 Temperature

Temperature profiles (Figure 17) were calculated at the top of the conduit at $t=1$ yr. They are plotted across the 2.5 m half-conduit and 0.5 m into the host rock (x-axis). Initial temperature profiles are shown for reference.

Temperature changes range from $\Delta T=-592$ K in which the dike is cooling to $\Delta T=313$ K in which shear heating is prominent ($\Delta T=T_{max}-T_0$). The highest temperatures occur in the outer 0.5 m of the conduit and are typically accompanied by significant temperature increases in the first 0.5 m of host rock (Figure 17). Figure 18 shows ΔT plotted within the parameter space. For $a=0.015$ K^{-1}, models with lower η_0 values (10^4 and 10^3 Pa s) were run in order to ensure that the model was acting realistically and to estimate the optimal viscosity for maximum shear heating. Decreasing from $\eta_0=10^7$ Pa s to $\eta_0=10^5$ Pa s, ΔT increases at each ΔP for $a=0.015$ K^{-1} (Figure 18a), but ΔT should not continue to increase with decreasing η_0 indefinitely because shear heating depends on both shear rate and viscosity. Indeed, ΔT does

decrease from $\eta_0=10^4$ Pa s to $\eta_0=10^3$ Pa s for $a=0.015$ K^{-1}. For $a=0.015$ K^{-1}, maximum ΔT occurs at the parameter combinations of $\eta_0=10^5$ and 10^4 Pa s with $\Delta P=30$ MPa. The lower η_0 limits of the maximum ΔT zone were not found for $a=0.02$ and 0.025 K^{-1}.
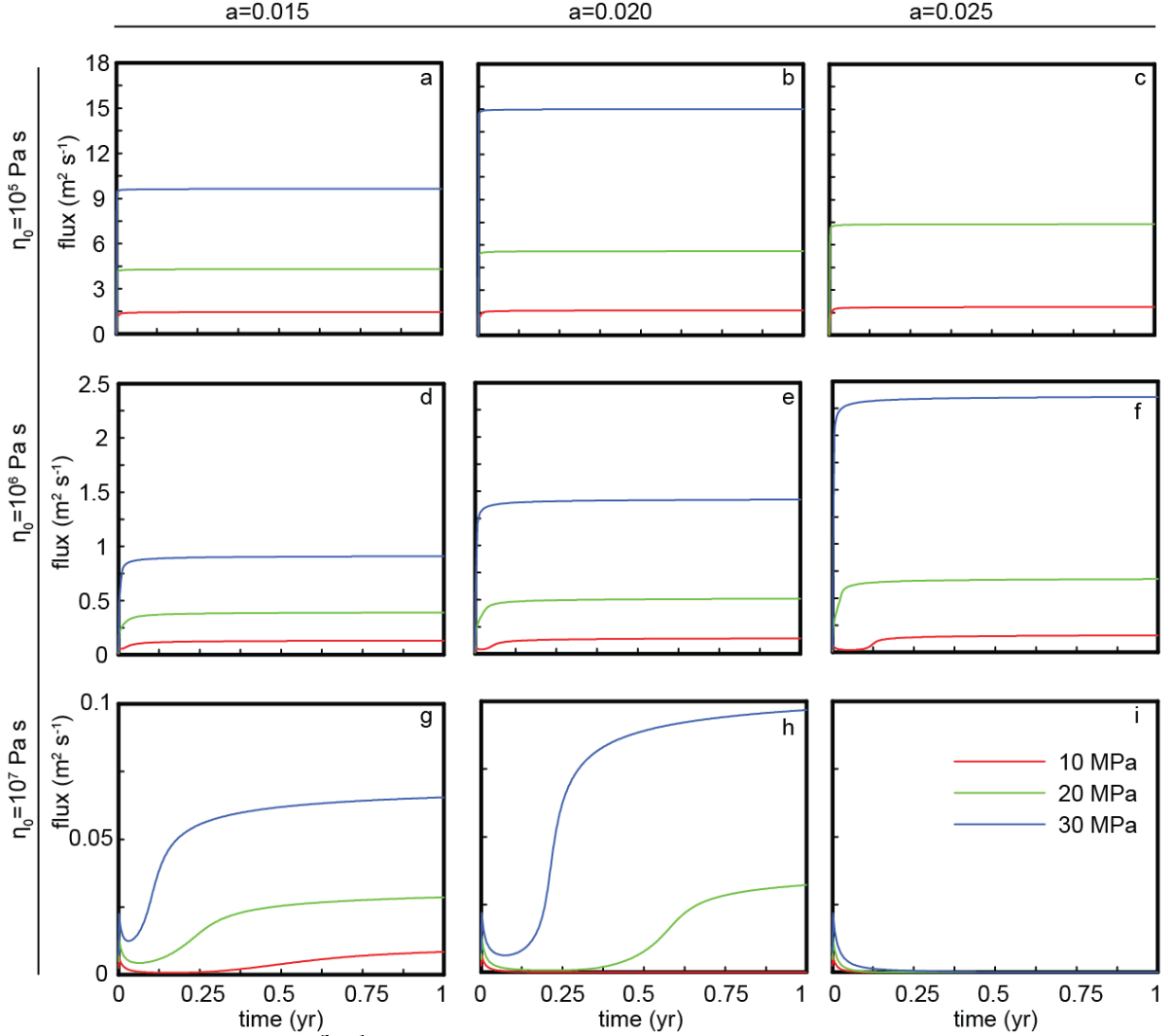
Figure 16. Flux (y-axis, m^2 s^{-1}) through time (x-axis, yr) for all 26 models. Models in (i) go to 0 m^2 s^{-1} almost immediately. Flux was calculated by integrating the velocity over the conduit exit for 500 time steps in the 1 yr model run time. Models either reach a steady state immediately, decrease to a flux minimum before increasing, or decrease to 0 immediately.
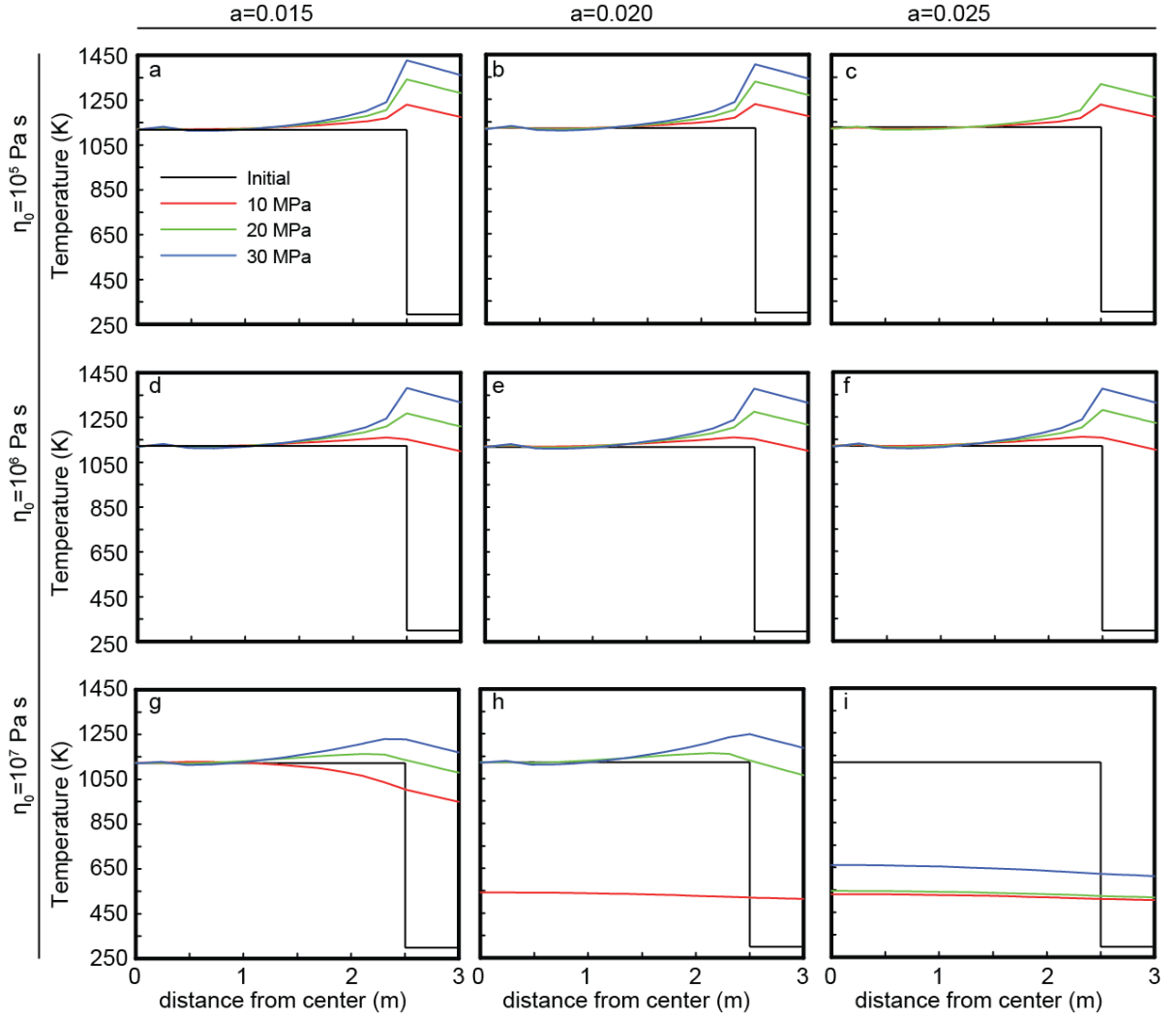
Figure 17. Temperature profiles within the 2.5 m half-conduit and 0.5 m into the host rock. Initial temperature profiles are shown for reference. Temperature profiles are shown for t=1 yr at the top of the conduit. Initial temperature profiles are shown for reference.
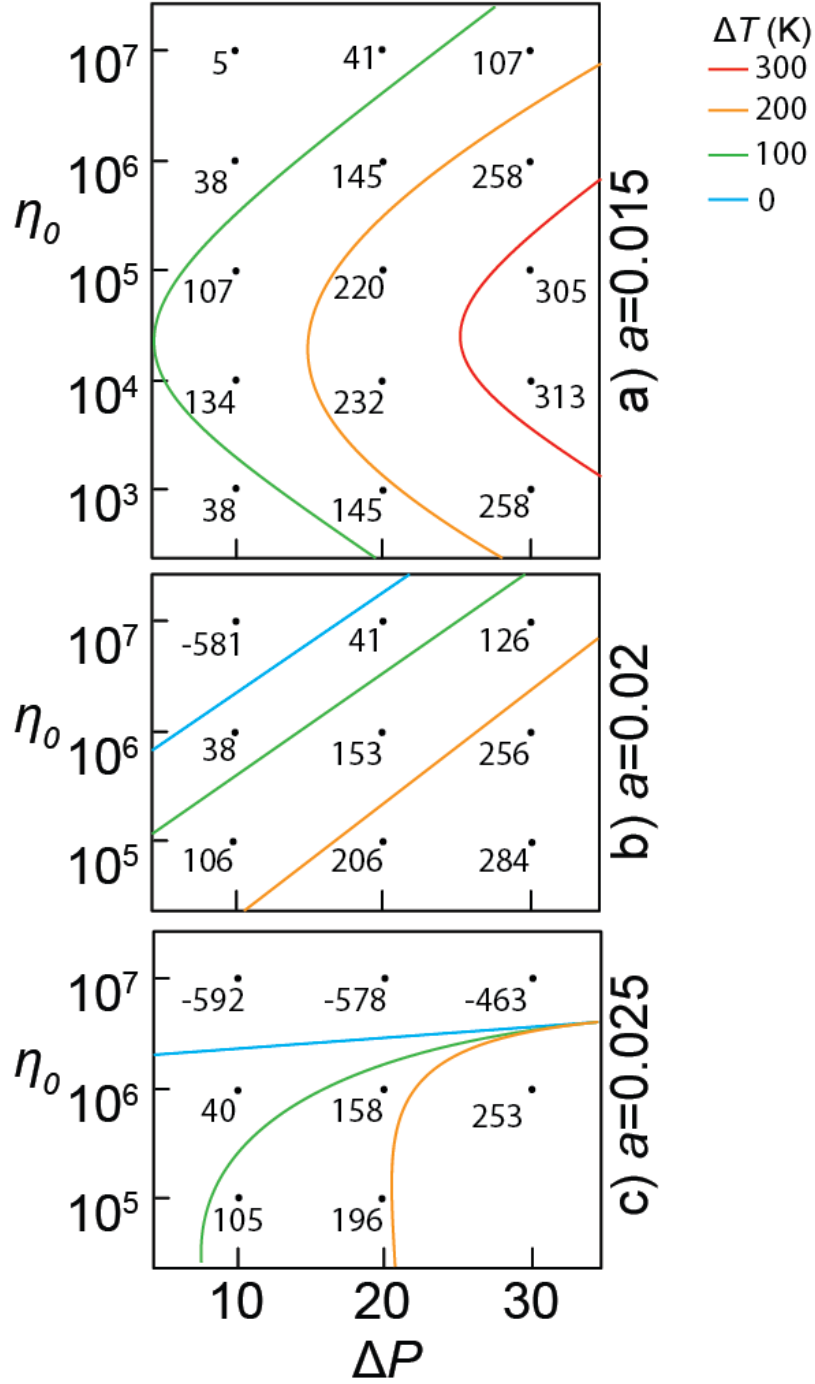
Figure 18. ΔT (K) contours plotted in the parameter space of η_0 (y-axis), ΔP (x-axis), and a values. Each point is the ΔT ($\Delta T = T_{max}-T_0$) for that model run. (a) Models with $a = 0.015$ K^{-1}. Models with lower η_0 values were run to ensure physical accuracy of model runs. At lower viscosities (10^4-10^3 Pa s), ΔT decreases as expected. (b) Models with $a = 0.02$ K^{-1}. (c) Models with $a = 0.025$ K^{-1}. Higher ΔT occurs at 10^6-10^4 Pa s and $\Delta P = 30$ MPa. Note that at $\eta_0 = 10^7$ Pa s, ΔT gets lower with higher a.

Table 6. Thermal Model Summary

Table 6a. ΔT (K)				Table 6b. Q_{final} (m^2 s^{-1})				Table 6c. u/u_{pois} (max)			
$\eta_0=10^5$ Pa s				$\eta_0=10^5$ Pa s				$\eta_0=10^5$ Pa s			
ΔP (MPa)	10	20	30	ΔP	10	20	30	ΔP	10	20	30
a (K^{-1})				a				a			
0.015	107	220	305	0.015	1.46	4.31	9.64	0.015	2.81	5.68	9.97
0.02	106	206	284	0.02	1.65	5.58	15.00	0.02	3.55	8.25	17.15
0.025	105	196		0.025	1.87	7.38		0.025	4.42	11.85	
$\eta_0=10^6$ Pa s				$\eta_0=10^6$ Pa s				$\eta_0=10^6$ Pa s			
ΔP (MPa)	10	20	30	ΔP	10	20	30	ΔP	10	20	30
a (K^{-1})				a				a			
0.015	38	145	258	0.015	0.13	0.39	0.91	0.015	1.83	4.26	8.75
0.02	38	153	256	0.02	0.14	0.51	1.42	0.02	2.11	6.54	15.64
0.025	40	158	253	0.025	0.16	0.68	2.35	0.025	2.46	9.87	28.19
$\eta_0=10^7$ Pa s				$\eta_0=10^7$ Pa s				$\eta_0=10^7$ Pa s			
ΔP (MPa)	10	20	30	ΔP	10	20	30	ΔP	10	20	30
a (K^{-1})				a				a			
0.015	5	41	107	0.015	0.01	0.03	0.07	0.015	0.93	1.73	3.95
0.02	581	41	126	0.02	0	0.03	0.10	0.02	0	1.85	7.14
0.025	592	578	463	0.025	0	0	0	0.025	0	0	0

Table 6. Summary of Figures 14-18. (a) Lists $\Delta T= T_{max}-T_0$ in which T_{max} is the maximum temperature plotted in Figure 17. (b) Lists Q_{final}, the flux value at $t=1$ yr (Figure 16). (c) Lists the maximum u/u_{pois} value from Figure 15.

4.3.4 Model behavior through time

To understand model behavior through time, 2 models are examined: 1) a model that reached a steady flux (Type 1; Figure 19) and 2) a model whose flux was still increasing at $t=1$ yr (Type 2; Figure 20). A closer look at temperature and velocity behavior through time is important to give a clearer picture of the dynamics of model behavior. The Type 1 model examined is the $\Delta P=10$ MPa, $\eta_0=10^5$ Pa s, and $a=0.015$ K^{-1} run (Figure 16a; Figure 19). The Type 2 model examined is the $\Delta P=20$ MPa, $\eta_0=10^7$ Pa s, and $a=0.015$ K^{-1} run (Figure 16g; Figure 20).

Temperature (Figure 19a) and velocity (Figure 19b) profiles of the Type 1 model develop towards the final state almost immediately. There is little initial cooling of the dike, even at this top part of the conduit. One interesting feature of this result is the time delay

between the velocity profile reaching its final state and the temperature profile reaching its final state. The velocity profile is fully developed after 36 days, but the temperature profile is still developing after 145 days (Figure 19). Thus, fully developed velocity (and by extension flux) values do not necessarily correspond in time to fully developed temperature profiles.

In contrast, temperature (Figure 20a) and velocity (Figure 20b) profiles of a Type 2 model decrease significantly before increasing to their final state. The top of the dike undergoes significant cooling during the first 36 days, and this temperature decrease is reflected in both the velocity (Figure 20b) and the flux (Figure 16g). At t=1 yr, the model evolved to a certain state, but the flux is still increasing, so Type 2 models require t>1 yr to reach a steady state.

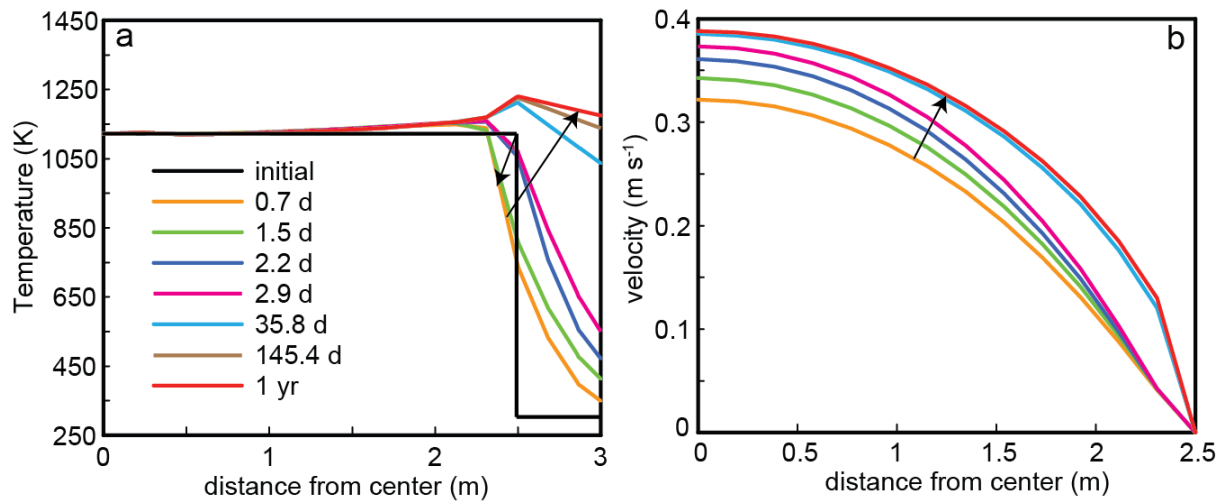Figure 19. Temperature (a) and velocity (b) profiles for a Type 1 model which reaches a steady flux state (see Figure 16a). Parameters are $\eta_0 = 10^5$ Pa s, ΔP=10 MPa, and a=0.015 K^{-1}. Arrows show behavior through time. Note that even though the velocity reached its approximate final state after only 36 days, the temperature is still increasing in the host rock after 145 days.
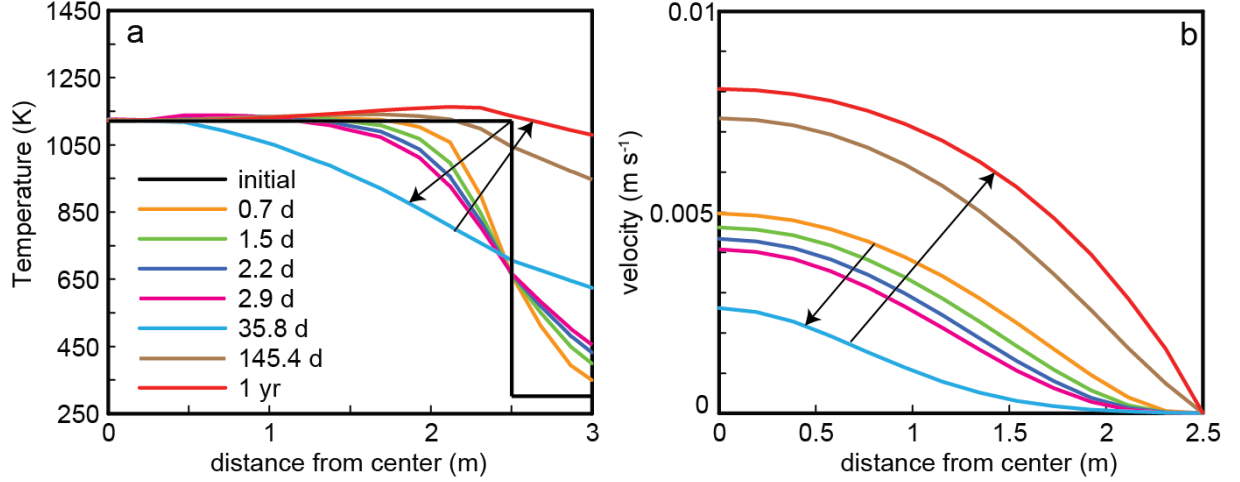
Figure 20. Temperature (a) and velocity (b) profiles of a Type 2 model. Parameters are $\eta_0=10^7$ Pa s, $\Delta P=20$ MPa, and $a=0.015$ K^{-1}. The initial cooling in (a) for at least 36 days is reflected in the velocity (b) and the flux (see Figure 16g). The dike overcomes this by advection of hotter material from below and shear heating of the conduit edges. Arrows show behavior through time.

Temperature changes with depth in the conduit yield another perspective on the thermal evolution through time. Figures 21 and 22 show temperature-depth profiles through time for the same models as Figures 19 and 20, respectively, at horizontal distances of x=1 m and 2.4 m from the center of the conduit. Initial time profiles t=0.73, 1.46, 2.19, and 2.92 d are more jagged than later time steps in Figures 21b and 22b. This change from intense temperature swings in the first time steps to more stable temperature profiles shows the model numerically stabilizing. Temperatures in Figure 21a vary within 5° of T_0, so the profiles are actually somewhat stable during the entire model run. The general shape of each profile is due to the set temperature at the bottom of the conduit (T_0) and the combined effects of advection of hot material from below, shear heating, and cooling by conduction in the rest of the conduit.

For the Type 1 model, the temperature does not change significantly at x=1 m, but does change significantly at x=2.4 m (Figure 19a). This is reflected in Figure 21a (x=1 m), in which temperature does not vary significantly with depth during the duration of the model (<

34

5 K). This is also reflected in Figure 21b, which shows the initial cooling at this horizontal distance. By t=35.8 d, the temperature profile has exceeded T_0 due to shear heating.

For the Type 2 model, the temperature changes significantly at both x=1 and x=2.4 m (Figure 20a) due to the increased viscosity. At x=1 m (Figure 22a), the dike temperature increases slightly at the initial time steps (< 15 K) and then cools significantly by t=35.8 d. The temperature then increases significantly by t=145.4 d before slightly decreasing to t=1 yr. At x=2.4 m (Figure 22b), the dike undergoes a much more significant temperature decrease, to < 800 K before rebounding and reaching a final temperature higher than T_0. This shows how a dike thermally recovers from initially intense cooling.
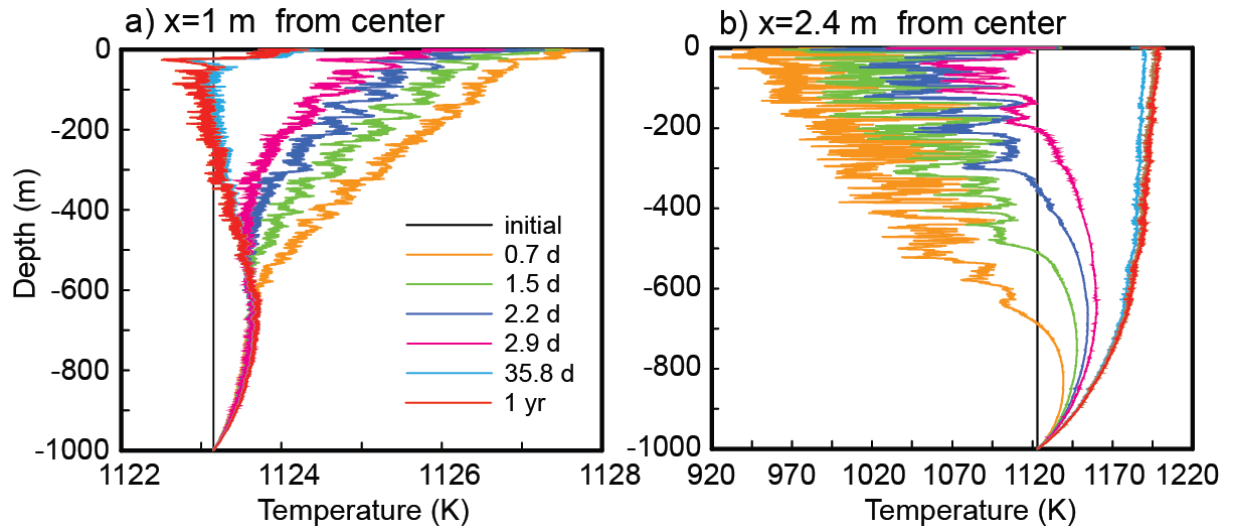
Figure 21. Type 1 model with η_0=10^5 Pa s, ΔP=10 MPa, and a=0.015 K^{-1} (same as Figure 19). Temperature (x-axis, K) is plotted with depth in the conduit (y-axis, m) for 1 m (a) and 2.4 m (b) from the conduit center. The large temperature irregularities in the initial time steps (t=0.7, 1.5, 2.2, 2.9 d) disappear by t=35.8 d in (b). Profiles in (a) look irregular, but the dike experiences little temperature variation (~5 K), which makes sense based on Figure 19a. The general shape of each profile is due to the set temperature at the base (T_0) and the combined effects of advection, shear heating, and conductive cooling in the rest of the dike.
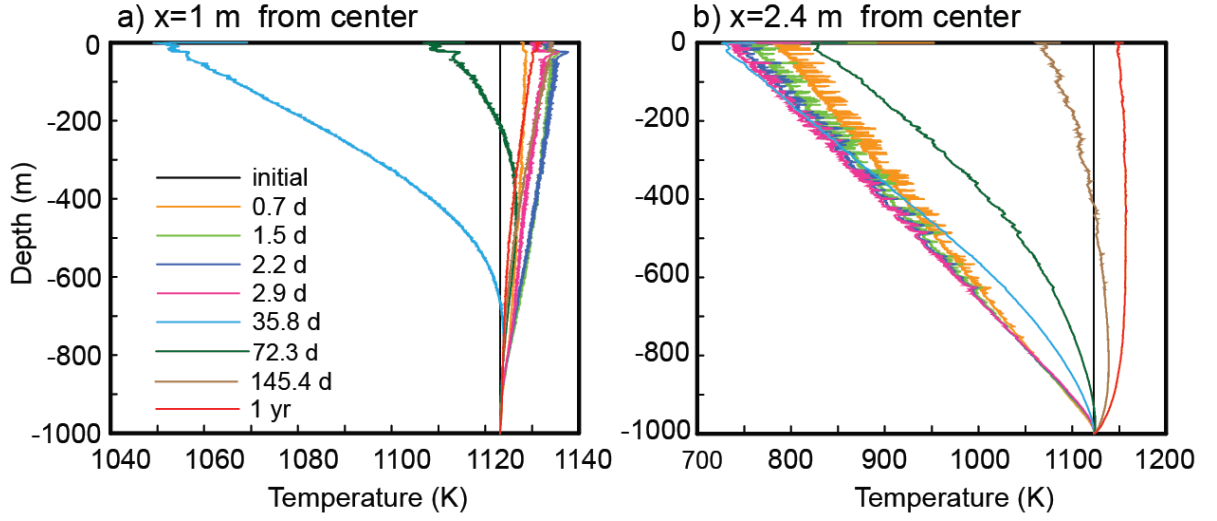
Figure 22. Type 2 model with $\eta_0=10^7$, $\Delta P=20$MPa, and $a=0.015$ K^{-1} (same as Figure 20). Temperature (x-axis, K) is plotted with depth in the conduit (y-axis, m) for x=1 m (a) and 2.4 m (b) from the conduit center. In contrast to Figure 21, the x=1 m profiles (a) show significant cooling by $t=35.8$ d. Severe cooling near the conduit edge at x=2.4 m (b) is overcome and eventually experiences temperatures $>T_0$. The general shape of each profile is due to the set temperature at the base (T_0) and the combined effects of advection, shear heating, and conductive cooling in the rest of the dike.

5. DISCUSSION

5.1 Thermal modeling

5.1.1 Shear heating

Velocity, flux, and temperature variation in the current study behave much like the numerical models of Costa et al. (2007) and Mastin (2005): 1) shear heating increases the temperature near the conduit edges but has little effect on the center of the conduit, 2) velocity profiles develop into more of a plug-like flow due to temperature increases at the edges, and 3) flux was able to reach values higher than the Poiseuille solution allows. Model temperatures in Mastin (2005) increased by 100 K in 600 s, whereas those in Costa et al. (2007) increased 150 K in 5 yrs. This study examined timescales intermediate to these studies and reached temperatures over 300 K higher than T_0 in less than a year. Host rock temperatures just outside the conduit also increase significantly in the 1 yr run time (Figure 17), indicating possible melting of wall rock. To what degree this actually melts the wall rock depends on kinetics and the duration of temperature increase. The same is true for crystal dissolution within the conduit.

Over the period of 1 yr, maximum temperatures in most models reached a steady state, meaning that thermal runaway defined as unbounded temperature increase did not occur despite extremely high G'' values (see Table 4). For the wide range of G'' values examined, ΔT remains below ~300 K (Figure 23a). In Figure 23, models group according to ΔP and η_0 in clusters of 3. Within each cluster, ΔT slightly decreases or increases with

37

increasing *a*. For models with $G''<300$, ΔT increases, whereas for $G''>300$, ΔT decreases with increasing *a*.

The lack of expected thermal runaway in this study is due to the fact that velocity and flux do not increase indefinitely in numerical models. Theoretical studies of thermal runaway (Gruntfest, 1963; Nelson, 1981) calculated ever-increasing velocities and fluxes at constant
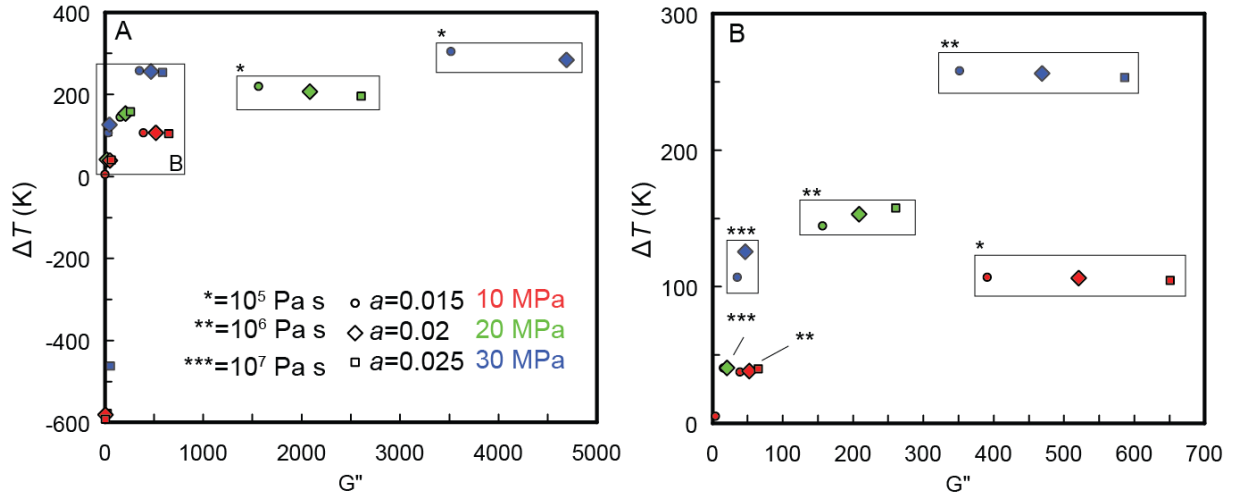
Figure 23. ΔT (K) plotted against modified Gruntfest number, G''. Models group according to ΔP and η_0. Within each cluster of 3, increasing *a* slightly decreases ΔT for $G''>300$. For $G''<300$, increasing *a* increases ΔT.

pressures because conduction away from the conduit could not keep up with viscous heat production. Higher temperatures within the conduit mean lower viscosities, higher velocities, and higher fluxes. The numerical models in this study show that for chosen parameters, which are consistent with these theoretical studies in addition to experimental and empirical data, velocity and flux do not increase indefinitely. Instead, a steady-state velocity and flux were reached, producing no thermal runaway.

5.1.2 Velocity and flux comparison

To compare flux values given in Figure 14 to observed volcanic eruptions, a third dimension, the horizontal dike length, is required. Dikes have high aspect ratios (e.g., Thomson et al.,

1995; Poland et al., 2004), and the dike inferred to connect the Inyo chain (Eichelberger et al., 1985) would need to be >1 km long (horizontally) to connect Obsidian Dome and Glass Creek. Using 3 representative fluxes from Figure 14 ($m^2 s^{-1}$), volumetric fluxes ($m^3 s^{-1}$) were calculated for horizontal lengths up to 1 km (Figure 24). A high (10 $m^2 s^{-1}$), medium (2 $m^2 s^{-1}$), and low (0.1 $m^2 s^{-1}$) flux were chosen (Figure 14). The dike in the present study is 5 m wide, yielding an aspect ratio of 200 with a 1 km horizontal length. Even at this somewhat low aspect ratio, model fluxes are extremely large compared to estimated fluxes at Mount St. Helens and Santiaguito (Figure 24a). Dome growth at Mount St. Helens from 1980-1983 was ~4 x 10^4 $m^3 d^{-1}$ (Swanson et al., 1987), whereas flux at Santiaguito ranged from ~2 x 10^4 to 2 x 10^5 $m^3 d^{-1}$ since 1922 (Harris et al., 2003). For a 1 km horizontal dike length, chosen model fluxes range from 8.6 x 10^6 to 8.6 x 10^8 $m^3 d^{-1}$, at least one order of magnitude larger than observed fluxes (Figure 24).

However, viscous magmas like those erupted from the Inyo chain or Mount St. Helens do not erupt along fissures that are kilometers in length. Instead, they erupt at centralized points owing to focusing of magma flow (MacDonald, 1943; Foshag and Reyna, 1956; Vogel et al., 1989). The Inyo Drilling Program reported a conduit 34.2 m across below Obsidian Dome interpreted to be a localization of magma connecting the feeder dike to the surface (Eichelberger et al., 1985; Vogel et al., 1987). From this measurement alone, the exact geometry of the conduit cannot be known. However, because it is a localization of magma flow, it can be assumed that each horizontal dimension is much smaller than horizontal length of the feeder dike (>1 km). Taking the Obsidian Dome conduit measurement into consideration, flux measurements calculated with ≤50 m as the long horizontal dimension (still 5 m wide) are closer to observed fluxes (Figure 24b).

39
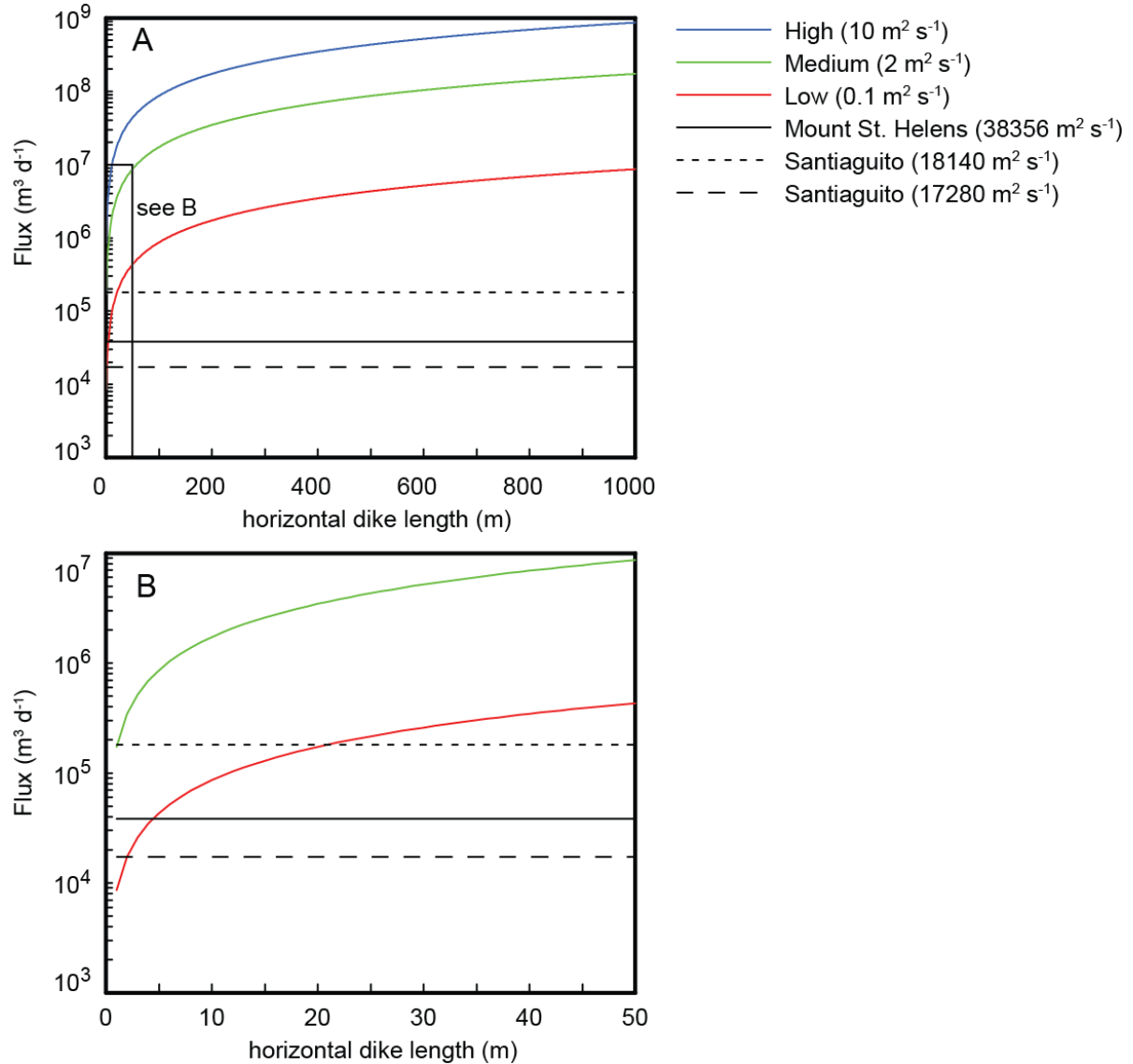
Figure 24. Flux (m^3 d^{-1}) as a function of horizontal dike length using high, medium, and low model fluxes (m^2 s^{-1}). Calculated fluxes are compared to observed fluxes at Mount St. Helens and Santiaguito (Swanson et al., 1987; Harris et al., 2003). Only at low horizontal dike lengths do these fluxes agree (b). Note that flux values for Mount St. Helens and Santiaguito are not functions of the horizontal dike length-they are estimates based on observations.

Velocity reaches maximum values of 3.3 m s^{-1} for η_0=10^5 Pa s models, 0.52 m s^{-1} for η_0=10^6 models, and 0.023 m s^{-1} for η_0=10^7 Pa s models. All except 5 models move at < 1 m s^{-1} (Figure 14). Most velocities fall between 10^{-2}-10^{-1} m s^{-1} (Figure 14), which is comparable to mean ascent rates of granitic magmas estimated with fluid dynamics (10^{-2} m s^{-1}; Petford et al, 1993). Other numerical models of magma ascent reported a wide range of values: 10-40 m

40

s^{-1} (Mastin, 2005) and 0.01-0.06 m s^{-1} (Costa et al., 2007). The large velocities in this study result from large overpressures (ΔP=30 MPa) and low viscosity (η_0=10^5 Pa s).

One reason for high velocities and fluxes in thermal models might be the lack of material building up at the top of the conduit as it would in an actual eruption. Lava accumulation at the conduit exit during volcanic eruptions increases the pressure at the top of the conduit, thereby decreasing ΔP given a constant inlet pressure (P_0). This decrease in ΔP means decreased velocity and flux. In models in this study, inlet and outlet pressure do not change based on what happens at the top of the conduit. Taking a realistic buildup of the volcanic edifice into account in thermal models might yield more realistic velocity and flux values.

5.2 Modal Mineralogy

Several differences exist between modal analyses in this study (Table 5) and previous studies (Table 1). Samples 01LM12 and 05COSO12A contain no phenocrysts instead of the reported phenocrysts from Table 1. Of samples containing phenocrysts, differences include: 1) Glass Mountain samples contain no quartz, sanidine, or biotite, 2) resurgent dome samples contain no quartz or biotite, and 3) Coso Dome 4 contains no sanidine or biotite. These differences are the product of the inherent difficulty of conducting modal analyses of obsidian.

The primary difficulty is the lack of crystals in obsidian. Some studies used mineral separates to assess mineral assemblages (e.g., Manley and Bacon, 2000), whereas others used thin sections (e.g., Kelleher, 1986). This inherent difficulty led to a dearth of quantitative modal data of crystal-poor obsidian in the literature. The modal mineralogy of individual

41

domes or flows was either qualitatively described (Metz and Mahood, 1991) or not reported (Bailey et al., 1976).

Despite these difficulties and discrepancies amongst data, the phenocryst data reported here, which show a lack of quartz and sanidine in CP obsidian (Table 5; Figures 7 and 8), reflect a broader theme across eastern California obsidian: quartz and sanidine are sparse to absent. In the Coso rhyolites, quartz is absent in 23 of 39 domes, and sanidine is absent in 10 domes (Manley and Bacon, 2000). At Glass Mountain, sanidine is sparse in some and absent in one of the younger, crystal-poor rhyolites (Metz and Mahood, 1991). In the resurgent dome, sanidine is absent altogether (Bailey et al., 1976). This regional lack of quartz and sanidine in crystal-poor obsidian is unusual because more crystal-rich, high-silica rhyolites contain these phases (e.g., Lipman et al., 1978; Johnson and Lipman, 1988; Christiansen, 2001).

Quartz and alkali feldspar comprise the equilibrium cotectic mineral assemblage for the haplogranite system (Figure 6). Assuming that an obsidian magma crystallized at this cotectic during its history, the absence of either quartz or sanidine indicates subsequent disequilibrium and resorption, or physical removal of the crystals. Rounded minerals are indicative of resorption processes (Donaldson, 1985; Streck, 2008), and CP obsidian contains dominantly rounded minerals compared to the few rounded minerals in CR obsidian. Causes of resorption include increased water content, higher temperatures, and changes in pressure (Tuttle and Bowen, 1958; Johannes and Holtz, 1996).

Increasing water content lowers the solidus, making it easier to melt phases at a given temperature and pressure (Johannes and Holtz, 1996, their Figure 2.13). However, this study found no evidence that obsidian was water-rich based on LOI (0.23-0.85 wt% except

01PB12, 1.9 wt%; Appendix B). Decompression generally induces crystallization in magmas (e.g. Figure 2.13 in Johannes and Holtz, 1996), but during decompression-driven crystallization in the haplogranite system (Figure 6), quartz becomes unstable and can resorb as the cotectic shifts towards the quartz apex (Blundy and Cashman, 2001). This can explain the presence of alkali feldspar without quartz in obsidian (e.g. some Coso domes, Manley and Bacon, 2000), but it cannot explain the lack of alkali feldspar (sanidine) in many obsidian domes and flows.

The thermal models in this study indicate that shear heating can produce large temperature increases in high-silica magmas. The ability of this temperature increase to resorb phenocrysts is discussed below.

5.3 Crystal resorption by shear heating

The amount of time a crystal experiences elevated temperature is important to understanding the possibility of crystal resorption. Models in this study have a wide range of velocity profiles that vary through time and along the x-axis, but the important velocities are in the outer 0.5 m of the conduit where the temperature increase is taking place (Figure 17). The term 'edge velocity' is used here to denote the range of velocities in the outer 0.5 m of the conduit. With specific velocities in this range of velocities, a residence time in the conduit can be calculated to get a first-order understanding of the time crystals could be subjected to increased temperatures. Residence times represent the minimum time it takes a crystal to move through the conduit edge because each model started with slower velocities.

This study used a 1 km conduit, but residence times were also calculated for longer conduits because magmas travel from deeper levels (e.g., Manley and Bacon, 2000). Of the 23 models with non-zero velocities, only 4 models have edge velocities >1 m s^{-1}. For these

43

19 models with <1 m s^{-1} edge velocities, the residence time in a 1 km conduit ranges from ~1000 s (16.7 minutes) to 5 x 10^{6} s (~58 days). Residence time increases as the crystal gets closer to the edge of the conduit (decreasing velocity) and as the conduit length increases (Figure 25). In Figure 25, the entire range of model edge velocities was used to calculate the residence time (y-axis).
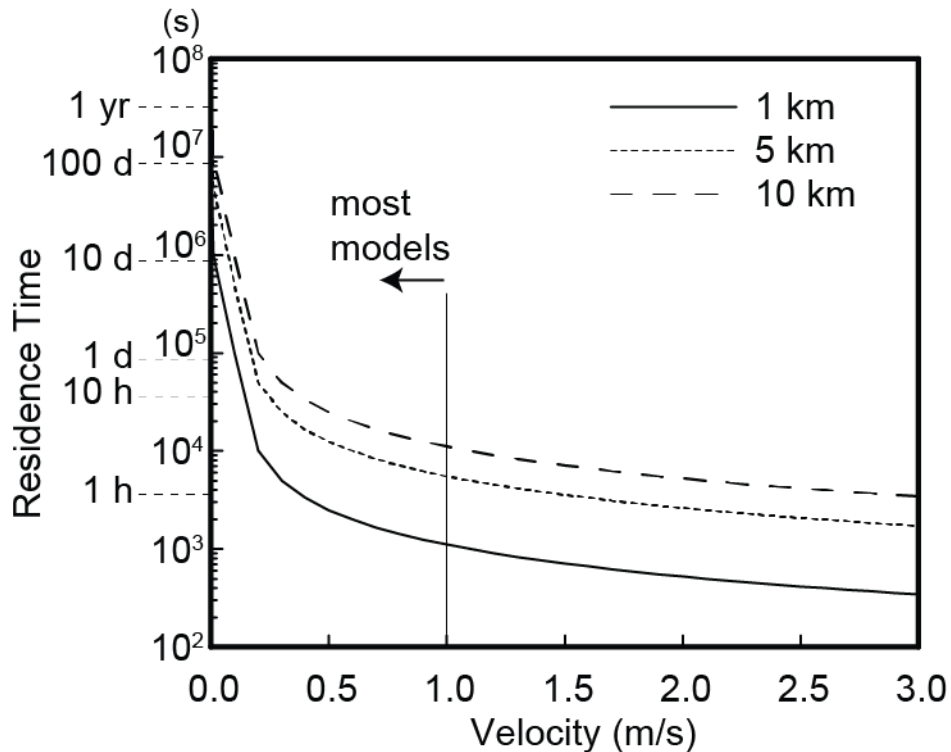
Figure 25. Residence time as a function of velocity (m s^{-1}) for crystals travelling in 1, 5, and 10 km conduits. For most models, edge velocities are <1 m s^{-1}, yielding minimum residence times of 16.7 minutes.

The temperatures experienced during conduit travel are important when considering crystal resorption. In Figure 26, residence time (x-axis) was calculated with specific velocities at x=2.3 m (from center) and t=1 yr in each model for a 1 km conduit. For simplicity, maximum temperatures at t=1 yr were used in Figure 26, meaning that part of the residence time was spent at lower temperatures. Figure 26 shows that as residence time increases, the maximum temperature reached decreases because of the relationship between

velocity, shear rate, and shear heating. Faster magma means more shear heating and shorter residence times. Crystal resorption is favored by high temperatures and longer residence time.
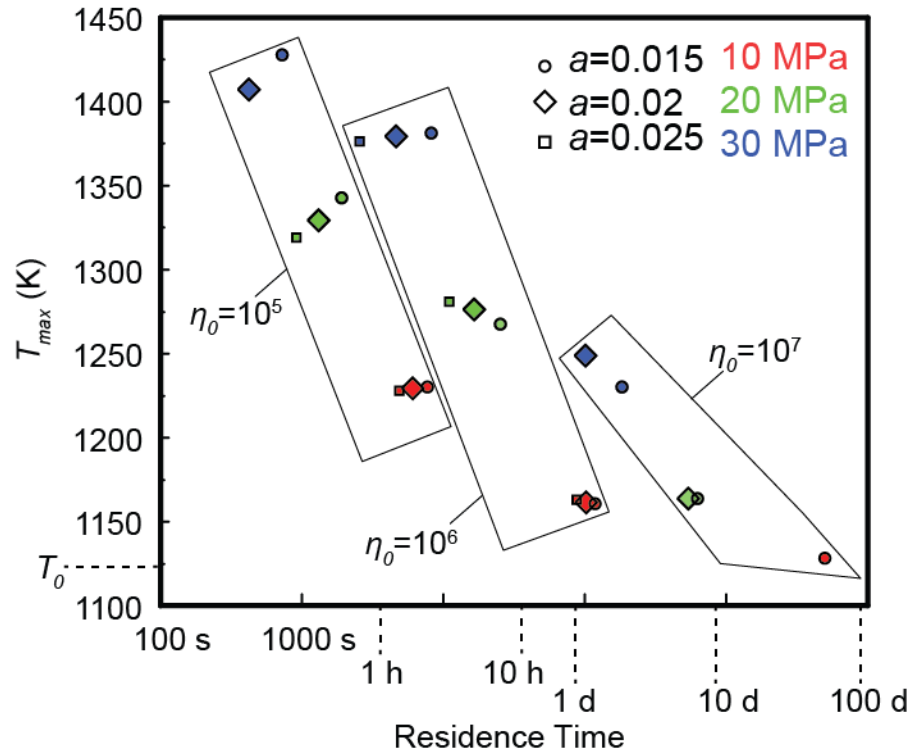
Figure 26. Residence time calculated with velocities at x=2.3 m and *t*=1 yr for a 1 km conduit plotted with T_{max} at *t*=1 yr. Different symbols represent different *a* values, and different colors represent each ΔP value. Polygons are drawn around models with equivalent η_0.

The pre-eruptive magmatic conditions of the Coso system range from 1013 K and 270 MPa (~10 km) to 1043 K and 140 MPa (~5.5 km) over the previous 0.6 Ma (Manley and Bacon, 2000). During this pre-eruptive period, sanidine and plagioclase are interpreted as being in equilibrium with the liquid, similar to many other rhyolites (e.g., Metz and Mahood, 1991). However, the notable lack of quartz and/or sanidine in eruptive deposits was not addressed by these authors. Somewhere between pre-eruptive storage and eruption, sanidine and/or quartz were lost.

Experimental studies of silicic systems combined with thermal modeling results presented in this study can shed some light on this discrepancy. Brugger et al., (2003) conducted experiments using compositions similar to obsidian (74-78 wt% SiO_2) at 1 atm (and therefore essentially water-free) to investigate phase relations. These authors found the equilibrium mineral assemblage to be plagioclase, quartz, orthopyroxene, and oxides at 1263-1523 K (990-1250° C) and 1 atm. This means that sanidine is unstable in high-silica magmas at near-surface pressures and high temperatures for these bulk compositions. Thus, if an ascending, silicic magma experiences thermal disequilibrium near the surface potentially caused by shear heating (Figures 17 and 26), sanidine could be resorbed. Whether or not an ascending magma experiences quartz resorption as discussed earlier (section 5.2), sanidine resorption, or some of both depends on the intensity of decompression versus shear heating during ascent. The equilibrium mineral assemblage given by Brugger et al. (2003) is from an experimental run, so rapid decompression of magma is not a factor and cannot cause quartz resorption.

Even though temperature increases of 200-300 K (Figure 26) are significant, their short duration and limited extent within the conduit seem to make crystal resorption implausible as a significant process. To resorb all of the sanidine in an ascending magma, which is necessary to produce an entire dome lacking in sanidine, heat needs to be transferred to the center of the conduit as well. Models in this study show high temperatures only in the margins of the dike. Furthermore, resorption of crystals depends upon not only reaching high temperatures, but upon the kinetics of crystal dissolution once high temperatures are reached. In the absence of kinetic data on rates of crystal dissolution during heating of silicic magmas,

it is unclear whether or not minerals could melt in the high-temperature margins of the model dike.

Natural systems, however, are much more complex. The 'balloon-and-straw' version of a magma chamber and dike leading to the surface is not realistic for the majority of volcanic or plutonic systems. Instead, a complex network of discrete dikes transfers magma to the surface (e.g., Donnelly-Nolan, 1988; Benz et al., 1996). Complexities in dike geometry can lead to separation of laminar flow (Taneda, 1979), which could be a possible mechanism for high-temperature flow lines to effectively transfer heat to other parts of the dike. Taking into account longer travel distances also increases chances for crystal resorption (Figure 25).

6. CONCLUSIONS

Modal analyses of crystal-poor obsidian reveal a lack of sanidine and quartz. Thermal disequilibrium caused by shear heating during ascent could explain the lack of sanidine and the rounded crystals present in crystal-poor obsidian. Thermal models do not experience thermal runaway but do increase >300 K from T_0 at the conduit edge due to shear heating. Models with higher ΔP, lower a, and 10^4-10^5 Pa s viscosities produced larger temperature increases. Model fluxes approach observed eruption fluxes at low horizontal lengths (<50 m), and most model velocities are < 1 m s^{-1}. Residence time in heated magma at the conduit edge is inversely related to the maximum temperature reached because higher temperature decreases viscosity and increases velocity in the conduit. Resorption is favored by high temperatures and longer residence times. Producing whole obsidian domes lacking in sanidine requires increased temperatures throughout the dike, not just the edges. Complex dike geometries in natural systems could help distribute high temperatures to magma throughout the dike, and longer travel distances would increase residence time in hotter magma. Though more complex dike geometries and longer dike lengths need to be examined in COMSOL, results indicate that shear heating can have a significant effect on the thermal budget of ascending silicic magma and could be the cause for the observed mineralogy of obsidian.

APPENDIX A. COMSOL BENCHMARKING

Analytical solutions of Equations 6-7 were used to benchmark COMSOL Multiphysics. Heat flow (Equation 6) in COMSOL was tested against the 1-dimensional heat flow equation given by Spear (1993, Equation 3-10),

$$\frac{dT}{dt} = \kappa \frac{\partial^2 T}{\partial x^2} + \frac{A}{\rho C_p} - u_x \frac{dT}{dx}, \qquad \text{Equation (A1)}$$

in which A is internal heat production (W m^{-3}) and κ is thermal diffusivity ($k\, C_p^{-1}\, \rho^{-1}$). The solution to Equation A1 for conduction only is (Spear, 1993, Equation 3-29),

$$T' = \frac{T - T_s}{T_0 - T_s} = \frac{1}{2}\left(erf\left(\frac{h - x}{2\sqrt{\kappa t}}\right) + erf\left(\frac{h + x}{2\sqrt{\kappa t}}\right) \right), \qquad \text{Equation (A2)}$$

in which T_s is the host rock temperature and *erf* is the error function.

Figure A1 compares the analytical solution (A) with the COMSOL solution (B), and Table A1 compares the maximum dimensionless temperature (*T'*) values at each time step. COMSOL handles heat conduction with precision when compared to the analytical solution.
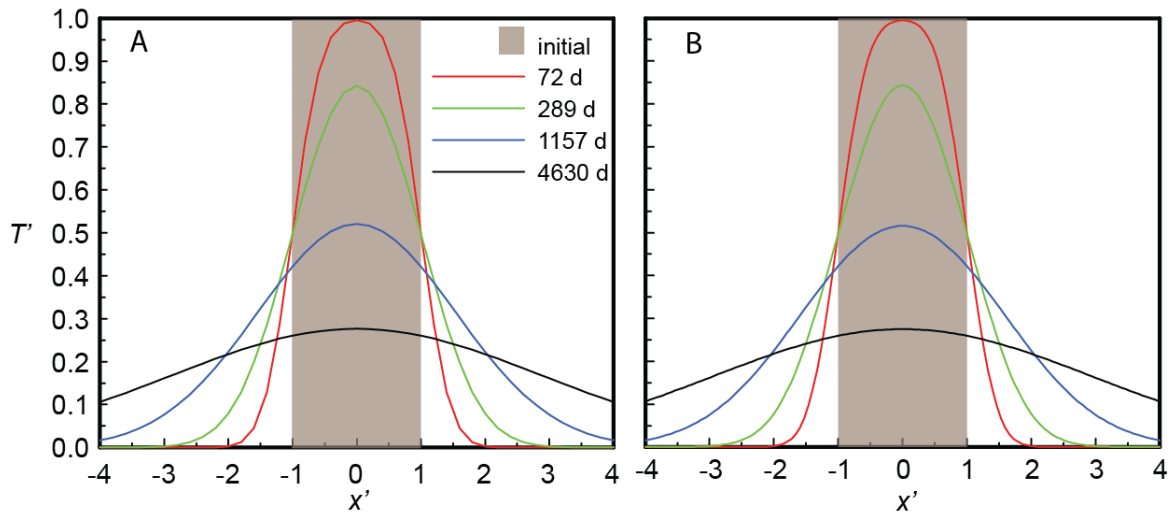

Figure A1. Comparison of the analytical (a) and COMSOL (b) solutions to the 1-D heat equation for conduction only. COMSOL replicates the analytical solution almost exactly. See Equations A1-A2 for the analytical solution.

Table A1. Heat Benchmark

Time (days)	T'_{max} (Equation A2)	T'_{max} (COMSOL)
72	1	0.995
289	0.84	0.84
1157	0.52	0.52
4630	0.28	0.28

Table A1. Maximum dimensionless temperature, T' (see Equation A2), for the analytical solution and the COMSOL solution at each time step.

Analytical solutions of Equation 7 for velocity and flux are, respectively,

$$u(x) = \left(\frac{dp}{dy}\right)\frac{h^2 - x^2}{2\eta} \qquad\qquad \text{Equation A3}$$

and

$$Q = \left(\frac{2}{3}\right)\left(\frac{dp}{dy}\right)\left(\frac{h^3}{\eta}\right) \qquad\qquad \text{Equation A4}$$

for flow through a planar dike, adapted from Equations 2.8 and 2.9 of Tritton (1988). Using

a 100 m long, 5 m wide dike with a magma viscosity of 7.78 x 10^4 Pa s, flux and velocity

were computed with Equations A3-A4 for different ΔP values. Table A2 compares these

analytical solutions to those calculated by COMSOL. COMSOL slightly underestimates flux

and velocity, but is accurate to within 0.9 m s^{-1} and 0.5 m^2 s^{-1}.

Table A2. Fluid Flow Benchmark

ΔP (MPa)	Predicted Q (m^2 s^{-1})	COMSOL Q (m^2 s^{-1})	Predicted velocity (m s^{-1})	COMSOL velocity (m s^{-1})
80	107.11	106.6	32.1332631	31.2
30	40.17	40.04	12.0501285	11.87
10	13.39	13.3	4.01670951	3.96

Table A2. Comparison of predicted velocity and flux from Equations A3-A4 using a 100 m long, 5 m wide conduit with a constant viscosity of 7.78 x 10^4 Pa s.

APPENDIX B. WHOLE ROCK DATA

Sample	Location	UTM (E,N)*	SiO_2	TiO_2	Al_2O_3	$Fe_2O_3^T$	MnO	MgO	CaO	Na_2O	K_2O	P_2O_5	Total	LOI (wt%)
01LM12	Resurgent Dome/ Lookout Mountain	328417, 4177444	74.632	0.166	13.642	1.359	0.039	0.125	0.72	3.873	5.17	0.005	99.731	0.4
01CD11	Resurgent Dome/ Casa Diablo	332863, 4167655	75.034	0.189	13.649	1.384	0.035	0.196	0.874	3.817	5.237	0.028	100.443	0.54
01ACD11	Resurgent Dome/ Casa Diablo	332863, 4167655	74.131	0.222	13.69	1.392	0.038	0.197	0.852	3.673	5.168	0.003	99.366	0.62
02CD11	Resurgent Dome/ Casa Diablo	333128, 4168032	74.713	0.183	13.709	1.375	0.038	0.183	0.875	3.75	5.195	-0.015	100.006	0.24
MAMM-1	Resurgent Dome/ Casa Diablo		74.692	0.195	13.907	1.405	0.038	0.197	0.874	3.784	5.176	-0.018	100.25	0.42
04GM11	Glass Mountain	349775, 4181707	77.267	0.09	12.703	0.796	0.036	0.033	0.405	3.963	4.774	-0.014	100.053	0.5
02AGM11	Glass Mountain	349234, 4181857	78.2	0.067	12.711	0.808	0.033	0.055	0.442	4.046	4.765	0.007	101.134	0.68
02GM11	Glass Mountain	349234, 4181857	77.659	0.062	12.704	0.8	0.033	0.038	0.434	3.981	4.813	0.005	100.529	0.85
03GM11	Glass Mountain	349159, 4181846	77.712	0.073	12.711	0.799	0.034	0.03	0.428	3.871	4.799	0.007	100.464	0.79
01PAN12A	Mono/ Panum Crater	320145, 4199723	76.378	0.084	12.88	1.17	0.049	0.03	0.507	4.043	4.723	-0.001	99.863	0.5
01D812A	Mono/ Dome 8	320718, 4197969	75.516	0.084	12.727	1.168	0.049	0.053	0.513	4.009	4.705	-0.016	98.808	0.38
01PB12	Mono/Punch Bowl	322037, 4187309	76.626	0.08	12.778	1.174	0.05	0.046	0.513	3.942	4.669	-0.015	99.863	1.93
02OD11	Inyo/ Obsidian Dome	321684, 4180037	75.207	0.189	13.75	1.369	0.035	0.172	0.859	3.795	5.216	0.027	100.619	0.59
01OD11	Inyo/Obsidian Dome	321659, 4180889	73.633	0.151	14.355	1.778	0.058	0.117	0.721	4.351	5.358	-0.002	100.52	0.6

APPENDIX B. WHOLE ROCK DATA (CONT.)

Sample	Location	UTM (E,N)*	SiO_2	TiO_2	Al_2O_3	$Fe_2O_3^T$	MnO	MgO	CaO	Na_2O	K_2O	P_2O_5	Total	LOI (wt%)
02GC12A	Inyo/Glass Creek	321699, 4179418	72.067	0.197	14.957	2.078	0.068	0.251	0.941	4.569	5.177	0.001	100.306	0.24
9-8-9	Coso/Dome 4	429200, 3994000	76.666	0.076	12.754	1.01	0.036	0.035	0.387	4.333	4.475	-0.019	99.753	0.41
05COSO12A	Coso/ Dome 16	427038, 3988840	76.593	0.078	12.691	1.121	0.034	0.008	0.39	4.346	4.577	-0.005	99.833	0.56

Note: Oxide values are in wt%. All Fe is reported as Fe_2O_3. LOI is loss on ignition. *Positions reported in UTM Zone 11, NAD83.

APPENDIX C. MODAL ANALYSES

Sample	Location	Obsidian (Y or N)	CP or CR	Area analyzed (cm^2)	Area % phenocrysts	Phases present*
01LM12	Resurgent Dome/ Lookout Mountain	Y	CP	26	0	NA (± ap, oxides)
02CD11	Resurgent Dome/ Casa Diablo	Y	CP	24	0.4	plg (92 %), opx (8%) ± bt, ap, pyr, zr, oxides
04GM11	Glass Mountain	Y	CP	20	0.2	plg ± bt, ap, zr, pyr, oxides
02AGM11	Glass Mountain	Y	CP	26	0.2	plg
01PAN12A	Mono/ Panum Crater	Y	CP	26	0	NA (± ap, oxides)
01D812A	Mono/ Dome 8	Y	CP	26	0.1	qz (54 %), plg (46 %)
01PB12	Mono/Punch Bowl	N	CR	24	5.1	See Table 1
02OD11	Inyo/ Obsidian Dome	Y	CR	25	9.4	See Table 1
02GC12A	Inyo/Glass Creek	Y	CR	24	2.4	See Table 1
05COSO12A	Coso/ Dome 16	Y	CP	29	0	NA
9-8-9	Coso/Dome 4	Y	CP	26	1.1	plg (59 %), qz (41 %) ± zr, ap, oxides

*Percent of dominant minerals given in parentheses.

APPENDIX D. QUANTITATIVE MINERAL DATA

This electronic appendix contains one Excel spreadsheet with quantitative mineral data used in this study collected on the JEOL JXA-8530F field emission electron probe microanalyzer at the Southeastern North Carolina Regional Microanalytical and Imaging Consortium at Fayetteville State University with the help of Nick Foster. In addition to mineral data used in this study, points collected on the volcanic glass in some samples are also tabulated. Each separate sheet within this spreadsheet contains data from one sample and type of mineral (e.g., 02CD11_feldspar or MAMM-1_pyroxene). Data collected on different dates are given within each sheet if data was collected on different dates. Standardization procedures were completed and tested each day of operation. Crystal names (i.e. 'feldspar1') within each sample are specific to the date under which they appear. In other words, 'feldspar1' from 02/07/13 is not necessarily the same crystal as 'feldspar1' from 02/21/13. For feldspar analyses used in this study, complete cation totals range from 4.98-5.02, and K+Na+Ca cation totals range from 0.98-1.02. For pyroxene analyses used in this study, complete cation totals range from 3.98-4.02, and Fe+Mg+Ca totals range from 1.97-2.02.
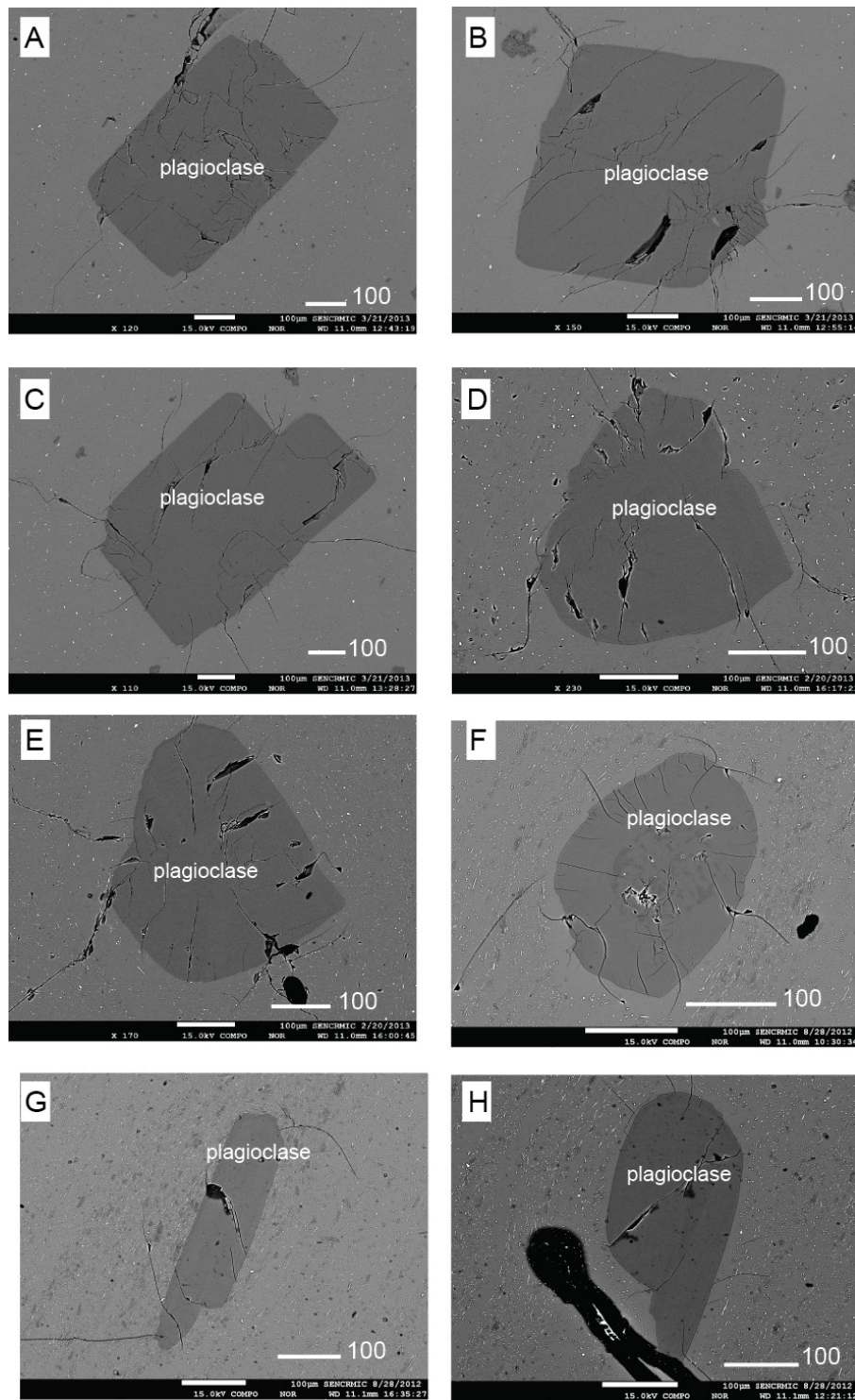
Figure D1. Backscattered electron images of plagioclase from CP obsidian. Scales are in micrometers. A-C are from 02AGM11, Glass Mountain; D-E are from MAMM-1 and F-H are from 02CD11, both from the resurgent dome. Images were collected on a JEOL JXA-8530F field emission electron probe microanalyzer.
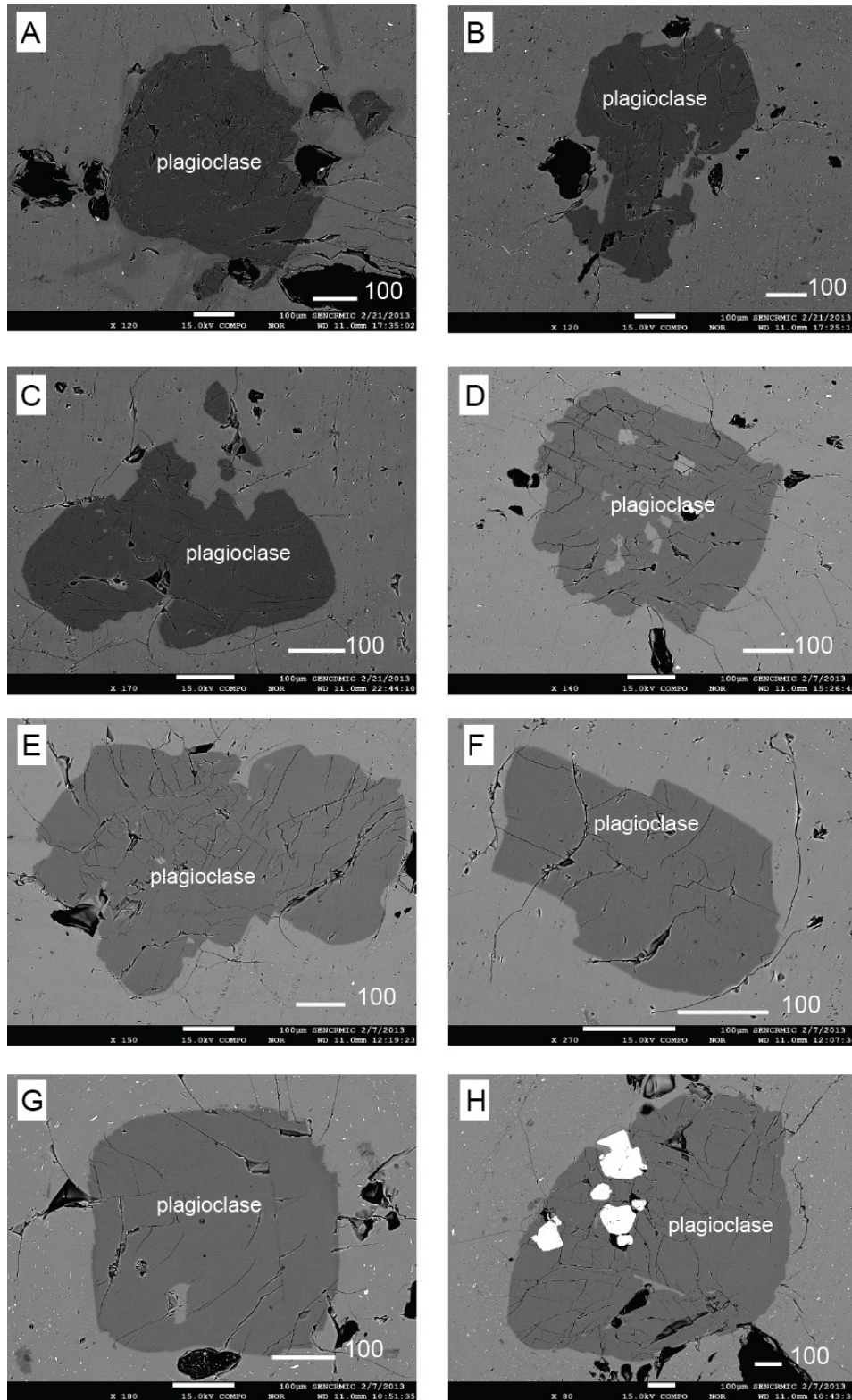
Figure D2. Backscattered electron images of plagioclase from CP obsidian. Scales are in micrometers. A-F are from 9-8-9, Coso Dome 4; G-H are from 01D812A, Mono Dome 8. Images were collected on a JEOL JXA-8530F field emission electron probe microanalyzer.
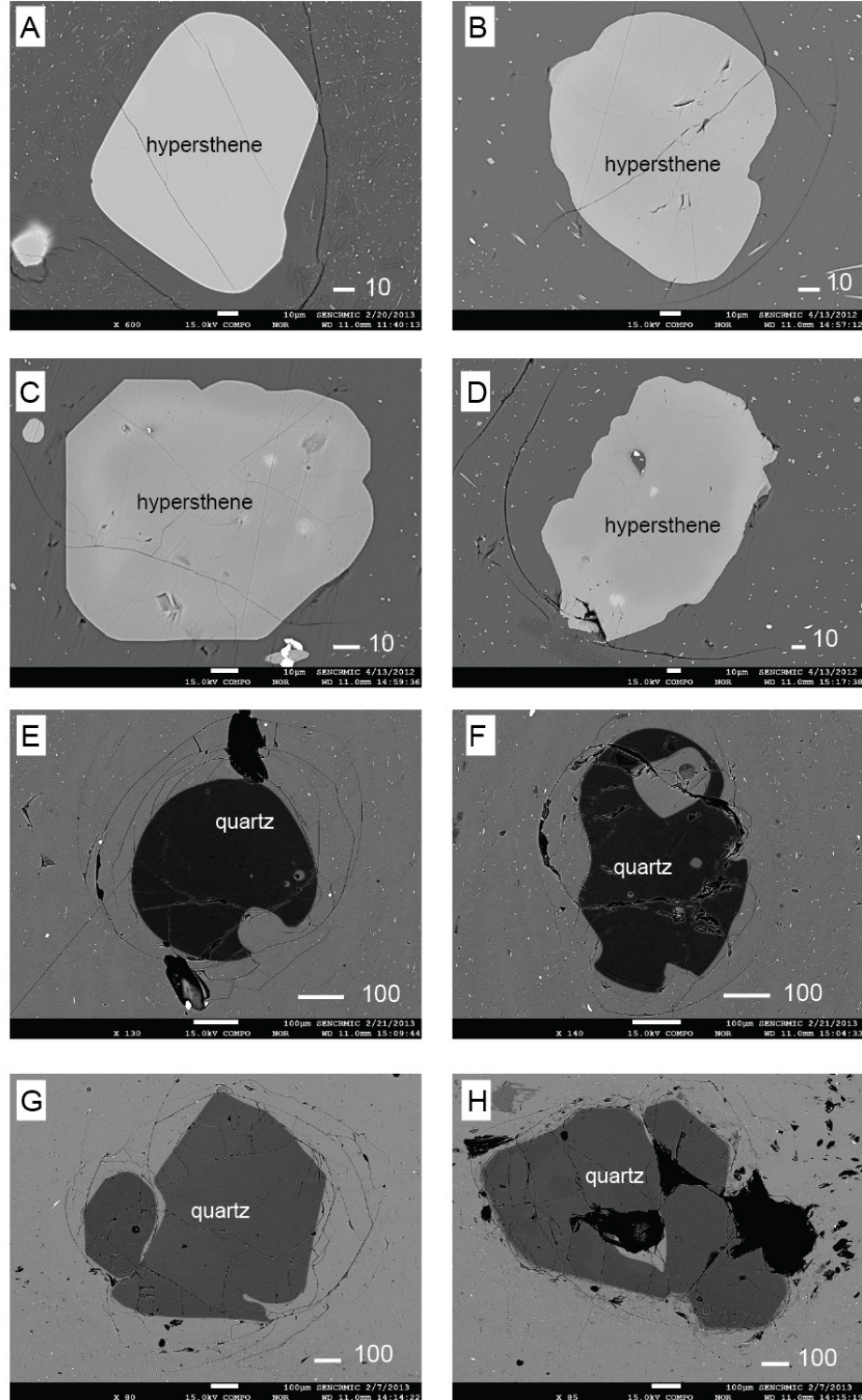
Figure D3. Backscattered electron images of hypersthene (A-D) and quartz (E-H) from CP obsidian. Scales are in micrometers. A-D are from either MAMM-1 or 02CD11, the resurgent dome; E-F are from 01D812A, Mono Dome 8; and G-H are from 9-8-9, Coso Dome 4. Images were collected on a JEOL JXA-8530F field emission electron probe microanalyzer.

Figure D4. Backscattered electron images of plagioclase and sanidine from CR obsidian. Scales are in micrometers. A is from 02OD11, Obsidian Dome (Inyo); B-E are from 02GC12A, Glass Creek dome (Inyo); and F-H are from 01P B12, Punch Bowl (Mono). Images were collected on a JEOL JXA-8530F field emission electron probe microanalyzer.

REFERENCES

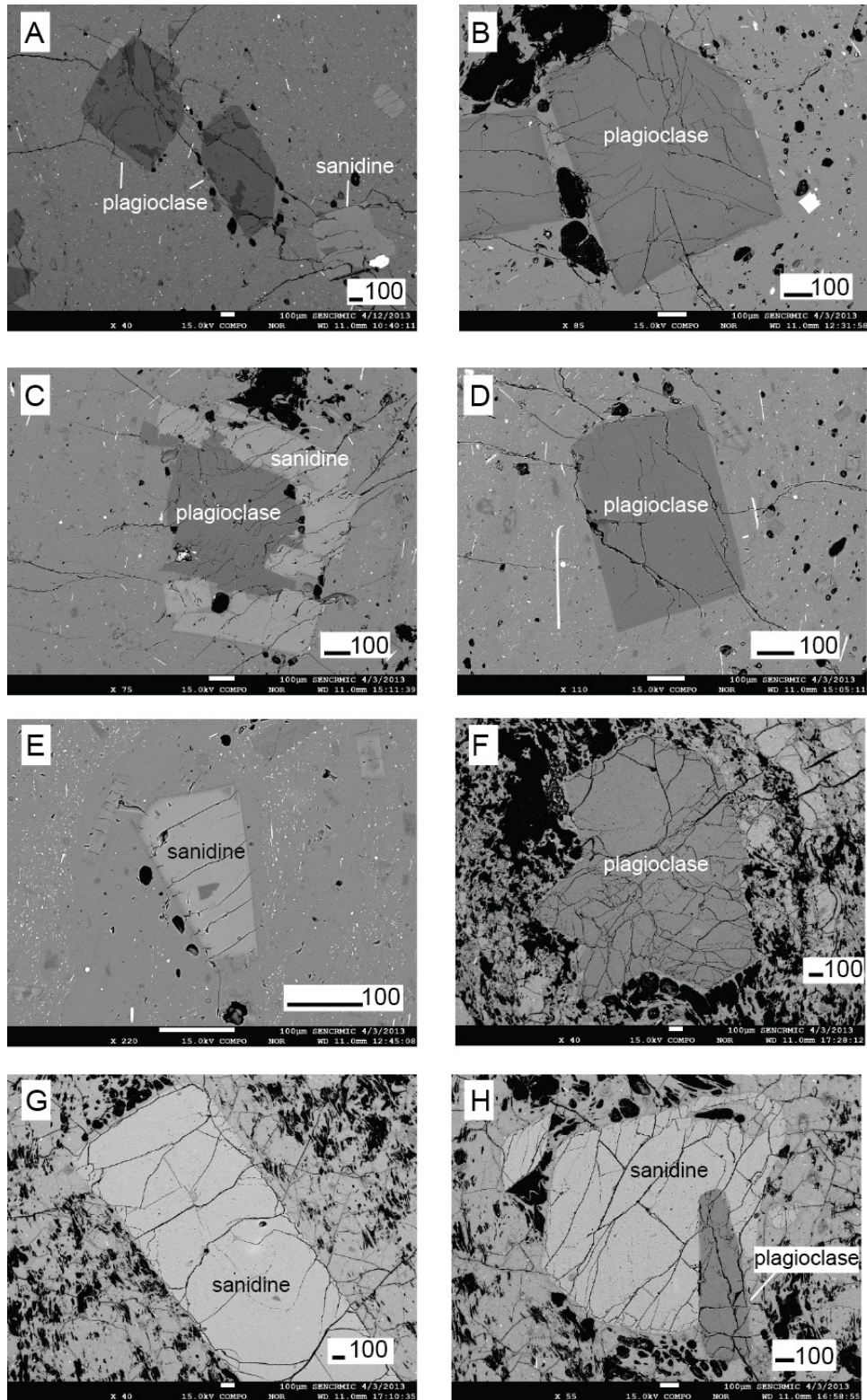Bacon, C.R., 1982. Time-predictable bimodal volcanism in the Coso Range, California. Geology 10, 65–69.

Bacon, C.R., MacDonald, R., Smith, R.L., Baedecker, P.A., 1981. Pleistocene High-Silica Rhyolites of the Coso Volcanic Field, Inyo County, California. Journal of Geophysical Research 86, 10223–10241.

Bailey, R.A., 1989. Geologic Map of Long Valley Caldera, Mono-Inyo Craters Volcanic Chain, and Vicinity, Eastern California. United States Geological Survey Miscellaneous Investigations Series Map I-1933, 2 sheets.

Bailey, R.A., Dalrymple, G.B., Lanphere, M.A., 1976. Volcanism, Structure, and Geochronology of Long Valley Caldera, Mono County, California. Journal of Geophysical Research 81, 725–744.

Baker, D.R., Vaillancourt, J., 1995. The low viscosities of F + H_2O-bearing granitic melts and implications for melt extraction and transport. Earth and Planetary Science Letters 132, 199–211.

Batchelor, G.K., 1967. An Introduction to Fluid Dynamics. Cambridge University Press, New York.

Benz, H.M., Chouet, B.A., Dawson, P.B., Lahr, J.C., Page, R.A., 1996. Three-dimensional P and S wave velocity structure of Redoubt Volcano, Alaska. Journal of Geophysical Research 101, 8111–8128.

Blundy, J., Cashman, K., 2001. Ascent-driven crystallisation of dacite magmas at Mount St Helens, 1980-1986. Contributions to Mineralogy and Petrology 140, 631–650.

Brugger, C.R., Johnston, A.D., Cashman, K.V., 2003. Phase relations in silicic systems at one-atmosphere pressure. Contributions to Mineralogy and Petrology 146, 356–369.

Carle, S.F., 1988. Three-Dimensional Gravity Modeling of the Geologic Structure of Long Valley Caldera. Journal of Geophysical Research 93, 13237–13250.

Christiansen, R.L., 2001. The Quaternary and Pliocene Yellowstone Plateau Volcanic Field of Wyoming, Idaho, and Montana. United States Geological Survey Professional Paper 729-G, 145 pp.

Costa, A., Melnik, O., Vedeneeva, E., 2007. Thermal effects during magma ascent in conduits. Journal of Geophysical Research 112, 16 pp.

Crowley, J.L., Schoene, B., Bowring, S.A., 2007. U-Pb dating of zircon in the Bishop Tuff at the millennial scale. Geology 35, 1123–1126.

Dingwell, D.B., Hess, K.-U., Romano, C., 1998. Viscosity data for hydrous peraluminous granitic melts: Comparison with a metaluminous model. American Mineralogist 83, 236–239.

Donaldson, C.H., 1985. A comment on crystal shapes resulting from dissolution in magmas. Mineralogical Magazine 49, 129–132.

Donnelly-Nolan, J.M., 1988. A Magmatic Model of Medicine Lake Volcano, California. Journal of Geophysical Research 93, 4412–4420.

Duffield, W.A., Bacon, C.R., 1981. Geologic Map of the Coso Volcanic Field and Adjacent Areas, Inyo County, California. United States Geological Survey Miscellaneous Investigations Series Map I-1200.

Eichelberger, J.C., Lysne, P.C., Miller, C.D., Younker, L.W., 1985. Research drilling at Inyo domes, California: 1984 results. EOS American Geophysical Union Transactions 66.

Ewart, A., 1976. Mineralogy and chemistry of modern orogenic lavas-some statistics and implications. Earth and Planetary Science Letters 31, 417–432.

Foshag, W.F., Reyna, J.G., 1956. Birth and Development of Paricutin Volcano. United States Geological Survey Bulletin 965-D, 355–489.

Fujii, N., Uyeda, S., 1974. Thermal Instabilities During Flow of Magma in Volcanic Conduits. Journal of Geophysical Research 79, 3367–3369.

Giordano, D., Russell, J.K., Dingwell, D.B., 2008. Viscosity of magmatic liquids: A model. Earth and Planetary Science Letters 271, 123–134.

Gruntfest, I.J., 1963. Thermal Feedback in Liquid Flow; Plane Shear at Constant Stress. Transactions of the Society of Rheology 195–207.

Hale, A.J., Wadge, G., Mühlhaus, H.B., 2007. The influence of viscous and latent heating on crystal-rich magma flow in a conduit. Geophysical Journal International 171, 1406–1429.

Harris, A.J.L., Rose, W.I., Flynn, L.P., 2003. Temporal trends in lava dome extrusion at Santiaguito 1922–2000. Bulletin of Volcanology 65, 77–89.

Hausback, B.P., 1987. An extensive, hot, vapor-charged rhyodacite flow, Baja California. Geological Society of America Special Paper 212, 111-118.

Hess, K.-U., Dingwell, D.B., 1996. Viscosities of hydrous leucogranitic melts: A non-Arrhenian model. American Mineralogist 81, 1297–1300.

Higgins, M.D., Meilleur, D., 2009. Development and emplacement of the Inyo Domes Magmatic Suite, California: Evidence from geological, textural (CSD) and

geochemical observations of ash and lava. Journal of Volcanology and Geothermal Research 186, 280–292.

Johannes, W., Holtz, F., 1996. Petrogenesis and Experimental Petrology of Granitic Rocks. Springer, New York, 335 pp.

Johnson, C.M., Lipman, P.W., 1988. Origin of metaluminous and alkaline volcanic rocks of the Latir volcanic field, northern Rio Grande rift, New Mexico. Contributions to Mineralogy and Petrology 100, 107–128.

Kelleher, P.C., 1986. The Mono Craters-Mono Lake Islands Volcanic Complex, Eastern California: Evidence for Several Magma Types, Magma Mixing, and a Heterogeneous Source Region. M.S. Thesis, University of California Santa Cruz, 111 pp.

Kelleher, P.C., Cameron, K.L., 1990. The Geochemistry of the Mono Craters-Mono Lake Islands Volcanic Complex, Eastern California. Journal of Geophysical Research 95, 17643–17659.

Kendrick, J.E., Lavallée, Y., Ferk, A., Perugini, D., Leonhardt, R., Dingwell, D.B., 2012. Extreme frictional processes in the volcanic conduit of Mount St. Helens (USA) during the 2004–2008 eruption. Journal of Structural Geology 38, 61–76.

Lavallée, Y., Mitchell, T.M., Heap, M.J., Vasseur, J., Hess, K.-U., Hirose, T., Dingwell, D.B., 2012. Experimental generation of volcanic pseudotachylytes: Constraining rheology. Journal of Structural Geology 38, 222–233.

Lipman, P.W., Rowley, P.D., Mehnert, H.. H., Evans, S.H., Nash, W.P., Brown, F.H., Observatory, H.V., City, S.L., Naeser, C.W., 1978. Pleistocene rhyolite of the Mineral Mountains, Utah-geothermal and archeological significance. Journal of Research of the USGS 6, 133–147.

MacDonald, G.A., 1943. The 1942 eruption of Mauna Loa, Hawaii. American Journal of Science 241, 241–256.

Mankinen, E.A., Grommé, C.S., Dalrymple, G.B., Lanphere, M.A., Bailey, R.A., 1986. Paleomagnetism and K-Ar ages of volcanic rocks from Long Valley Caldera, California. Journal of Geophysical Research 91, 633–652.

Manley, C.R., Bacon, C.R., 2000. Rhyolite Thermobarometry and the Shallowing of the Magma Reservoir, Coso Volcanic Field, California. Journal of Petrology 41, 149–174.

Massol, H., Jaupart, C., 1999. The generation of gas overpressure in volcanic eruptions. Earth and Planetary Science Letters 166, 57–70.

Massol, H., Jaupart, C., 2009. Dynamics of magma flow near the vent: Implications for dome eruptions. Earth and Planetary Science Letters 279, 185–196.

Mastin, L.G., 2002. Insights into volcanic conduit flow from an open-source numerical model. Geochemistry Geophysics Geosystems 3, 18.

Mastin, L., 2005. The controlling effect of viscous dissipation on magma flow in silicic conduits. Journal of Volcanology and Geothermal Research 143, 17–28.

Mastin, L.G., Roeloffs, E., Beeler, N.M., Quick, J.E., 2008. Constraints on the Size, Overpressure, and Volatile Content of the Mount St. Helens Magma System from Geodetic and Dome-Growth Measurements During the 2004 – 2006+ Eruption. In: Sherrod, D.R., Scott, W.E., Stauffer, P.H. (Eds.), A Volcano Rekindled: The Renewed Eruption of Mount St. Helens, 2004-2006. U.S. Geological Survey Professional Paper 1750, pp. 461–488.

Melnik, O., Sparks, R.S.J., 1999. Nonlinear dynamics of lava dome extrusion. Nature 402, 37–41.

Melnik, O., Sparks, R.S.J., 2005. Controls on conduit magma flow dynamics during lava dome building eruptions. Journal of Geophysical Research 110, 1–21.

Melnik, O., Barmin, A.A., Sparks, R.S.J., 2005. Dynamics of magma flow inside volcanic conduits with bubble overpressure buildup and gas loss through permeable magma. Journal of Volcanology and Geothermal Research 143, 53–68.

Metz, J.M., Mahood, G.A., 1991. Development of the Long Valley, California, magma chamber recorded in precaldera rhyolite lavas of Glass Mountain. Contributions to Mineralogy and Petrology 106, 379–397.

Miller, C.D., 1985. Holocene eruptions at the Inyo volcanic chain, California: Implications for possible eruptions in Long Valley caldera. Geology 13, 14–17.

Murase, T., McBirney, A.R., 1973. Properties of Some Common Igneous Rocks and Their Melts at High Temperatures. Geological Society of America Bulletin 84, 3563–3592.

Nelson, S.A., 1981. The possible role of thermal feedback in the eruption of silicic magmas. Journal of Volcanology and Geothermal Research 11, 127–137.

Petford, N., Kerr, R.C., Lister, J.R., 1993. Dike transport of granitoid magmas. Geology 21, 845–848.

Plouff, D., Isherwood, W.F., Bacon, C.R., Duffield, W.A., Van Buren, H.M., 1980. Bulk Density and Magnetization Measurements of Samples from the Coso Range, California. United States Geological Survey Open-File Report 80-61, 5 pp.

Polacci, M., Papale, P., Rosi, M., 2001. Textural heterogeneities in pumices from the climactic eruption of Mount Pinatubo, 15 June 1991, and implications for magma ascent dynamics. Bulletin of Volcanology 63, 83–97.

Poland, M.P., Fink, J.H., Tauxe, L., 2004. Patterns of magma flow in segmented silicic dikes at Summer Coon volcano, Colorado: AMS and thin section analysis. Earth and Planetary Science Letters 219, 155–169.

Richet, P., Lejeune, A.M., Holtz, F., Roux, J., 1996. Water and the viscosity of andesite melts. Chemical Geology 128, 185–197.

Rinehart, C.D., Ross, D.C., 1964. Geology and Mineral Deposits of the Mount Morrison Quadrangle Sierra Nevada, California. United States Geological Survey Professional Paper 385, 106 pp.

Romine, W.L., Whittington, A.G., Nabelek, P.I., Hofmeister, A.M., 2012. Thermal diffusivity of rhyolitic glasses and melts: effects of temperature, crystals and dissolved water. Bulletin of Volcanology 74, 2273–2287.

Sampson, D.E., Cameron, K.L., 1987. The Geochemistry of the Inyo Volcanic Chain: Multiple Magma Systems in the Long Valley Region, Eastern California. Journal of Geophysical Research 92, 10403–10421.

Sieh, K., Bursik, M., 1986. Most Recent Eruption of the Mono Craters, Eastern Central California. Journal of Geophysical Research 91, 12539–12571.

Shaw, H.R., 1963. Obsidian-H_2O Viscosities at 1000 and 2000 Bars in the Temperature Range 700° to 900° C. Journal of Geophysical Research 68, 6337–6343.

Shaw, H.R., 1972. Viscosities of magmatic silicate liquids: an empirical method of prediction. American Journal of Science 272, 870–893.

Spear, F.S., 1993. Metamorphic Phase Equilibria and Pressure-Temperature-Time Paths. Mineralogical Society of America Monograph Series, Washington, D.C.

Stimac, J.A., Wark, D.A., 1992. Plagioclase mantles on sanidine in silicic lavas, Clear Lake, California: Implications for the origin of rapakivi texture. Geological Society of America Bulletin 104, 728–744.

Streck, M.J., 2008. Mineral Textures and Zoning as Evidence for Open System Processes. Reviews in Mineralogy and Geochemistry 69, 595–622.

Swanson, D.A., Dzurisin, D., Holcomb, R.T., Iwatsubo, E.Y., Chadwick, W.W., Casadevall, T.J., Ewart, J.W., Heliker, C.C., 1987. Growth of the lava dome at Mount St. Helens, Washington, (USA), 1981-1983. Geological Society of America Special Paper 212, 111-118.

Thomson, B., Aftalion, M., McIntyre, R.M., Rice, C., 1995. Geochronology and tectonic setting of silicic dike swarms and related silver mineralization at Candelaria, western Nevada. Economic Geology 90, 2182–2196.

Taneda, S., 1979. Visualization of Separating Stokes Flows. Journal of the Physical Society of Japan 46, 1935–1942.

Tritton, D.J., 1988. Physical Fluid Dynamics. Oxford Univeristy Press, New York.

Tuttle, O.F., Bowen, N.L., 1958. Origin of granite in the light of experimental studies in the system $NaAlSi_3O_8$-$KAlSi_3O_8$-SiO_2-H_2O. Geological Society of America Memoir 74, 153 pp.

Vogel, T.A., Younker, L.W., Schuraytz, B.C., 1987. Constraints on magma ascent, emplacement, and eruption: Geochemical and mineralogical data from drill-core samples at Obsidian dome, Inyo chain, California. Geology 15, 405–408.

Vogel, T.A., Eichelberger, J.C., Younker, L.W., Schuraytz, B.C., Horkowltz, J.P., Stockman, H.W., Westrich, H.R., 1989. Petrology and Emplacement Dynamics of Intrusive and Extrusive Rhyolites of Obsidian Dome, Inyo Craters Volcanic Chain, Eastern California. Journal of Geophysical Research 94, 17937–17956.

Williams, H., Turner, F.J., Gilbert, C.M., 1954. Petrography: An introduction to the study of rocks in thin sections. W.H. Freeman and Company, San Francisco.